Copyright© VCH Verlagsgesellschaft mbH. 1996

6 The Technology Transfer Process: Solutions to Industrial Problems

This chapter will give some basic information on structural and functional coatings widely applied to solve mechanical and frictional performance and maintenance problems in industry as well as to impart new functional properties to materials surfaces. The material covered here is by no means exhaustive but should elucidate some fundamental trends in coating design as well as illustrate various physical processes occuring during plasma spraying of wear- and corrosion-resistant coatings, thermal and chemical barrier coatings, bioceramic coatings and various functional coatings.

6.1 Wear- and Corrosion-resistant Coatings

These coatings are most frequently based on transition metal carbides (WC, TiC, Mo_2C, TaC, NbC, Cr_3C_2) and also some hard oxides (Al_2O_3, TiO_2, Cr_2O_3), metals (W, Mo, Ti, Ta) and alloys (NiCoCrAlY), and diamond. Since the melting temperatures of the carbides are extremely high, and oxidation/decarburization generally occurs at such high temperatures, pure carbide powders cannot be properly melted and deposited even in high enthalpy plasma jets. Instead, carbide particles are embedded into easily melted binder metals such as Ni, Co, Cr, and their mixtures and alloys, respectively. There are, however, restrictions to the use of binder metals. For example, B_4C VPS-coatings on graphite, and carbon fiber composites CFC or steel tiles were tested for walls of nuclear fusion reactors without the use of binder metals that would be activated by the high neutron flux [1].

6.1.1 Pure Carbides

Carbides with simple structures are considered interstitial compounds characterized by a strong interaction of metal to carbon: the small carbon atom is located in either an octahedral interstitial site or at the center of a trigonal prism within the close-packed transition metal atoms.

The crystal structures of the carbides under discussion are determined by the radius ratio $r = r_X/r_T$, where X = carbon and T = transition metal [2]. If $r < 0.59$, the metal atoms form very simple structures with close-packed cubic or hexagonal arrangement. The carbon atoms are situated at interstitial sites. Those interstitial sites must be somewhat smaller than the carbon atom because otherwise there will be insufficient bonding resulting in an essentially unstable structure [3]. The following monocarbides crystallize in the cubic B1 (NaCl) structure: TiC, ZrC, HfC, VC, NbC, TaC, WC. Although molybdenum carbide has an r-value of 0.556 its cubic phase is non-stoichiometric MoC_{1-x} with a low temperature α-form and a high temperature β-form. The more stable structure with higher hardness and wear resistance is Mo_2C that crystallizes in the hexagonal T_2C structure in which only half of the interstial sites are occupied by carbon. The same structure type is found for W_2C.

Although *titanium carbide* crystallizes only in the cubic B1 structure it has an extraordinarily wide compositional range, and is thus stable between $TiC_{0.97}$ and $TiC_{0.50}$. The melting point is 3067 °C near a composition $TiC_{0.80}$. *Tungsten carbide* is stable at room temperature as cubic α-WC that melts at 2867 °C. The hexagonal W_2C-phase melts at a slightly lower temperature of 2750 °C. As mentioned above, WC loses carbon at appreciable rate above 2200 °C and will form a surface layer of W_2C.

If $r > 0.59$, more complicated structures arise in which the transition metal atoms do not form a close-packed arrangement anymore. An example is chromium carbide whose complicated phase relationships include a peritectically melting cubic $Cr_{23}C_6$ high temperature phase, a hexagonal Cr_7C_3 phase, and a peritectically melting orthorhombic low temperature Cr_3C_2 phase (T_P = 1810 °C). All three phases show a narrow range of homogeneity. Precipitation-strengthening of Cr_3C_2 by formation of Cr_7C_3 due to decarburization may be the reason for the exceptional solid-particle erosion resistance of those coatings (see Sec. 6.1.2.3).

6.1.2 Cemented Carbides

Cemented carbides are composite materials of pure carbides with a binder metal of low melting point and high ductility. The principal use of these materials is to produce cutting tools, but plasma-sprayed coatings of cemented carbides enjoy wide applications as surface layers to protect an extraordinarily wide range of machinery and tools from wear, erosion and corrosion. The term refers to a carbide of group 4b–6b elements of the periodic table together in a metal matrix such as cobalt or nickel. Mixtures of these metals, also together with chromium are often utilized. The selection of the binder metal depends to a large extent on its ability to wet the surface of the carbide particles to ensure secure coating cohesion. Addition of TiC, TaC and NbC to WC/Co-cemented carbide causes important property changes in terms of surface reactivity and/or melting behavior. Such multicarbide materials may contain TiC–TaC–NbC solid solutions[1] that improve the oxidation resistance at high tem-

[1] In the American engineering literature on cemented carbide coatings the name columbium (symbol: Cb) instead of niobium is still used.

peratures as well as hardness and hot strength. Often such a modification of the hard phase content of the composite is augmented by incorporating chromium into the carbide mix or by modifying the binder phase, e.g. cobalt–chromium or chromium–nickel–cobalt alloys. Like the hardness the transverse rupture-strength of a coating can be strongly influenced by the binder metal content that can be varied by the degree of dispersion of the carbide and binder metal phase. It is evident that the starting spray powder must be highly homogeneous in the first place to avoid layering of the coating and thus introduction of potential weak zones. The corrosion resistance of cemented carbide coatings is determined by both the corrosion resistance of the carbide(s) and the binder metals. The latter are generally soluble in acids so that their corrosion performance limits the application of such coatings in operations where highly acidic solutions or gases occur. In such cases the design engineer often resorts to oxide ceramic coatings such as alumina. But although alumina is highly corrosion-resistant its low fracture toughness and compliance pose problems (see Sec. 6.1.3.1).

In addition to mixed carbides and carbide solid solutions, ternary complex carbides have been developed [4]. These hexagonal carbides T_2MC (T = group 3b–6b elements of the periodic table; M = group 2b, 3a–6a elements) are called H-phases. Their crystal structure has been determined for Cr_2AlC [5] and Ti_2AlC [6]. The latter was used as hard phase in a pseudo-alloy matrix together with a hard Ni–Cr–10B–Si alloy [7] to flame- and plasma-spray wear-resistant coatings onto steel [4]. Such tribological coatings show improved wear resistance.

6.1.2.1 Tungsten Carbide/Cobalt Coatings

These materials are widely applied in industry as wear-resistant coatings because of their high hardness and excellent abrasion resistance. Owing to the complex interactions of the spray powder with the plasma jet, the environment and the substrate material, the coating process requires careful control of the powder characteristics and the plasma parameters [8, 9]. The coating techniques applied comprise conventional flame spraying, HVOF techniques (D-Gun, Gator Gard, Jet Cote), arc spraying and plasma spraying including conventional APS, LPPS and VPS, respectively, reactive plasma spraying, UPS and more. Recent developments indicate that HVOF flame spraying yields coatings highly optimized in terms of density, hardness, adhesion strength and phase purity compared to APS or VPS methods [10, 11]. However, for the development of 'designer coatings' under exclusion of oxygen that may lead to coating degradation VPS is also being considered [12, 23].

The coatings deposited must be rather thin so as not to compromise given tolerances of the machined parts and tools. While for wear applications a high coating density is desired, sometimes this requirement must be relaxed. The surfaces of plungers and barrels of reciprocating and centrifugal pumps, for example, must be somewhat porous so that the lubricants can adhere [13]. Cobalt-based tungsten carbide coatings are most useful for achieving high sliding-wear resistance and better friction properties [14]. They can be used to prevent general wear, cavitation erosion, and also chemical corrosion of a variety of oil field equipment including protection against severe particle erosion of choke nozzles of tungsten carbide alloy that are

used to control high-velocity flow of heavy oil contaminated with sand [15]. This requires secure bonding of a thin layer (<10 μm) of compatible tungsten carbide-based material to the nozzle substrate [13]. As the nozzle is supposed to rotate within a steel sleeve, problems of clearance control must also be addressed. How sophisticated the present technology has become to protect these choke nozzles from failure due to severe erosion, corrosion and scaling caused by hot, corrosive fluids and sand is illustrated by a study performed by ESSO Resources Canada Limited [15] that concluded that the massive tungsten carbide/cobalt substrate is best protected by a system of a CVD titanium nitride coating of 10 μm thickness followed by a 7 μm alumina and then a boron diffusion coating. It is very obvious that a single conventional 'off the shelf' coating is not sufficient anymore to protect machinery from nonlinear effects of corrabrasion, i.e. the synergistic interaction of corrosive and abrasive destruction of the material. Also, while it is still common practice to develop coatings by establishing a set of spray parameters adapted to different substrates by making only minor modifications to parameter sets information obtained from the widespread literature on this subject, there is an increasing need to design coating/substrate systems as a single entity [16]. Since this requires optimization of coating properties, statistical multifactorial experimental designs should be applied (see Chap. 8).

Since proper adhesion of the WC/Co coatings requires an optimized D/d ratio (see Eq. (5-8)) and therefore optimized particle viscosity and velocity, the plasma enthalpy and thus the plasma temperature become the determining factors. The plasma jet temperature must be substantially higher than the melting point of cobalt (1495 °C) but not so high that the tungsten carbide undergoes decomposition [17] or η-carbide (Co_nW_mC) formation [18]. The changes a stoichiometric WC/Co powder is subjected to during thermal exposure in the plasma spray process is illustrated in Fig. 6-1 that shows the low carbon portion of the ternary phase diagram W–C–Co. The WC phase reacts with the Co melt (see Fig. 5-18) and loses carbon by reaction with oxygen in the flame. The composition of the coating matrix is close to the η-carbide phase Co_3W_3C. This phase presumably leads to a deterioration of the mechanical strength due to its brittleness. Furthermore, W_2C formed by decarburization of WC tends to embrittle the coating. Even though under VPS conditions due to the absence of oxygen the formation of W_2C can be completely suppressed [8, 17], carbon can evaporate and form mixed tungsten carbides [12]. Figure 6-2 shows how, with increasing spray distance and the associated increase of the residence time of the particles in the flame, the carbon loss and the oxygen pick-up increased and the Rockwell hardness, HRC, substantially decreased [18].

Suppression of the decomposition of tungsten carbide by selecting high plasma gas flow rates at reduced hydrogen content has been attempted [19]. However, even under those conditions trace amounts of oxygen contained in the plasma gas (up to 50 p.p.m.) or in voids of the spray powder can lead to oxidative processes under formation of $CoWO_4$ [17]. Decrease of decomposition of tungsten carbide with increasing gas volumes at the same energy level because of reduced dwell time has also been confirmed by Chandler and Nicoll [9]. They also found that the use of an argon/hydrogen plasma reduced dramatically the amount of remaining WC and a concurrent increase in M_6C (Co_3W_3C) and $M_{12}C_4$ ($Co_3W_9C_4$) phases. Such an in-

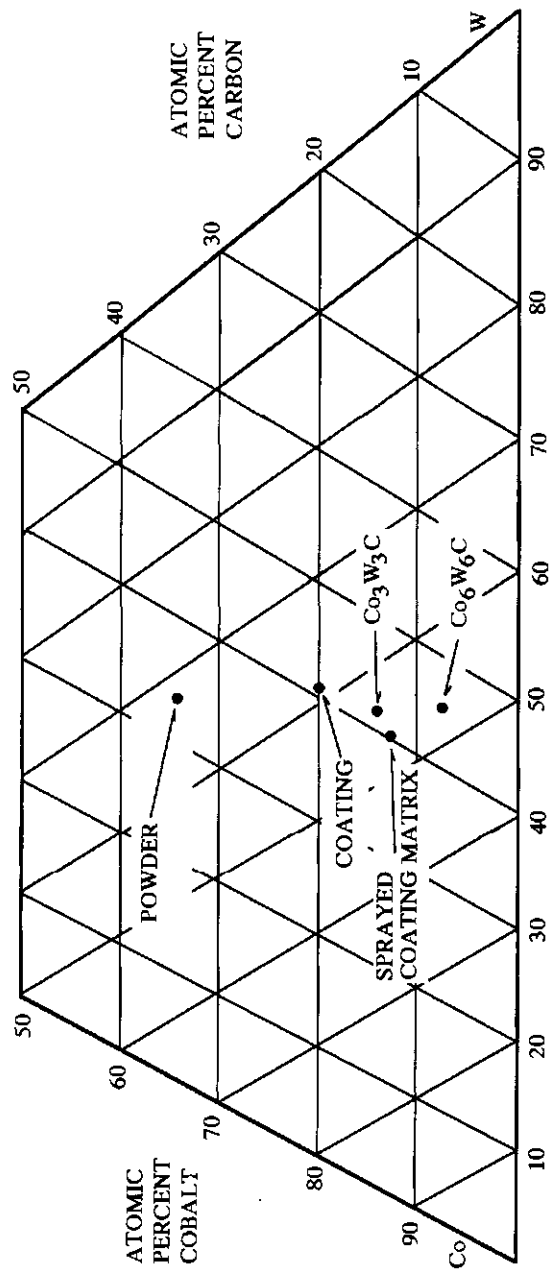

Figure 6-1. Low carbon portion of the ternary phase diagram W–C–Co showing the shift of the chemical composition of the starting powder towards the η-carbide phase Co_3W_3C during spraying [18].

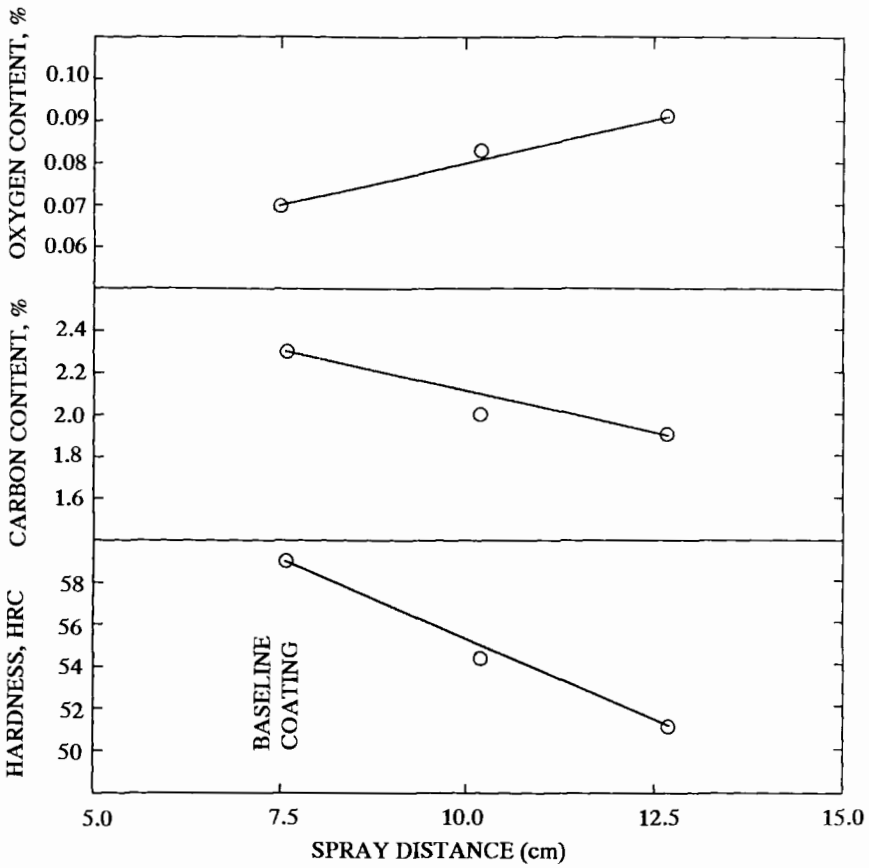

Figure 6-2. Oxygen pick-up, and carbon loss and decrease of the Rockwell hardness of WC–Co(Ni) coatings with increasing spray distance [18].

crease has been also observed with negative, i.e. upstream injection that has been found to disappear using positive, i.e. downstream injection. Again, the reduction of dwell time reduces decomposition.

Another way to suppress degradation of coating performance due to matrix-alloying is to inject separately the 88WC12Co phase and a Ni-based alloy (73Ni15Cr4Si4Fe3B1C) into a d.c. plasmatron with two injection ports [20]. The resulting composite coating deposited onto AISI 5150 steel is very dense and the carbide phase composition is close to that of the initial spray powder. In particular, decarburization products such as brittle W_2C and η-carbides are absent. The reason for this may be that with dual injection, the heat input to the carbide and the matrix metal can be independently tailored for optimum results by adjustment of the injection angles and locations as well as the plasmatron operating parameters.

The results of conventional co-spraying of a mechanical blend of 50WC50'A' (A = 73Ni15Cr4Si4Fe3B1C) onto very fine-grained powder-metallurgically densified tungsten carbide (88WC12NiCo) are shown in Figs 6-3 and 6-4. Figures 6-3a–c show cross-sections of the interfaces between the WC/NiCo substrate (left) and the 50WC50'A' coating (right) with X-ray line scans of tungsten (a), cobalt (b) and nickel (c). Figures 6-4a and b show the cracking behavior of the substrate/coating system subjected to a Charpy impact test. The main crack is situated within the fine-grained substrate (Fig. 6-4a) with a second crack running close to the interface but always within the substrate material. Figure 6-4b shows an enlarged view of the central area of Fig. 6-4a. In Fig. 6-4c a back-scattered image of the polished coating is shown illustrating the coarse-grained WC grains within the 'A' matrix [21]. Such tungsten carbide composite coatings were developed to combat severe solid-particle erosion (SPE) problems of choke nozzles in heavy crude oil production in the oil fields of Northern Alberta, Canada [15].

It has been mentioned above (see Sec. 6.1.2) that the modification of tungsten carbide by addition of highly refractory and extremely hard carbides such as TiC and TaC yields coatings with clearly improved wear resistance, frictional properties, and fracture toughness [22]. At low frictional velocities the wear resistance is rather low but increases with increasing velocities and therefore also temperatures [23]. This can be attributed to surface oxidation that decreases friction. In TiC-reinforced WC/Co coatings the TiC particles tend to collect near the surface of the coating owing to their low specific gravity thus creating a top layer that has an extremely good abrasion resistance.

The addition of TaC leads to three-phase alloys with improved high temperature properties in terms of oxidation and diffusion resistance against ferrous substrate materials [24].

Chemical degradation of the WC phase by oxidation, decarburization and matrix-alloying, as discussed above, yields coatings with noticeably decreased performance in terms of abrasion resistance. Coating microhardness may be, under simplified assumptions, indicative of abrasion resistance even though a proportionality between microhardness, and sliding and abrasive wear, respectively is rarely observed [25]. Much more important is the interaction of wear mode and microstructure of the coating. Spraying of WC/Co powder at high velocities in an inert atmosphere should considerably minimize the degradation of the WC/Co system. Indeed, experiments by Mutasim *et al.* [26] using a high velocity plasma spray process, modified with a plasmatron extension operating in a low pressure chamber (Fig. 6-5) pointed to a substantial decrease of the amounts of W_2C and Co_3W_3C and thus to an increase in microhardness approaching that of the powder-metallurgically densified 88WC12Co material (Fig. 6-6). It was concluded that the higher amounts of WC retained contributed to the observed increase in microhardness. Figure 6-7 shows a cross-section of a dense, well-adhering 88WC12Co wear coating (right) on a mild steel substrate (left) produced by APS with careful parameter optimization [13].

The hardness of the WC/Co composite depends strongly on the ratio WC to Co as well as, for monolithic materials, its grain size (Fig. 6-8). Therefore, different areas of application emerge.

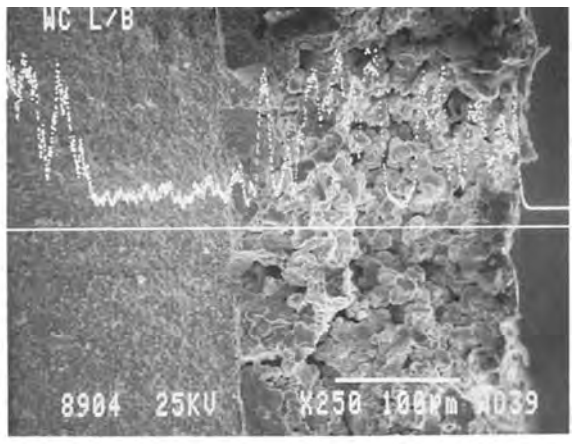

(a)

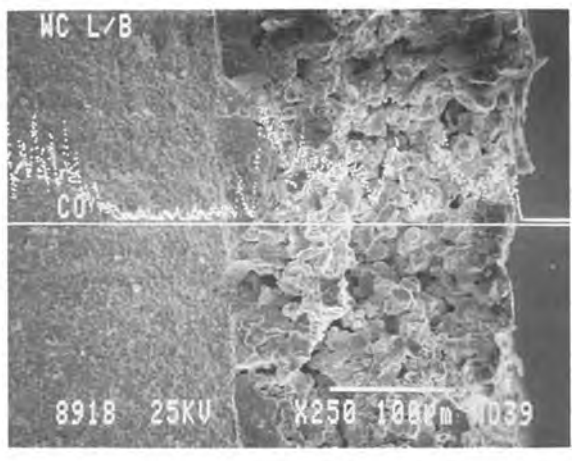

(b)

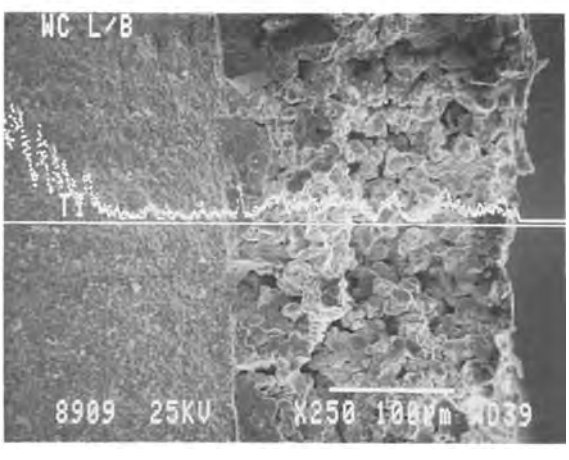

(c)

Figure 6-3. Tungsten carbide-based coating (right) on a fine-grained 88WC12NiCo substrate (left) with X-ray line scans of W(a), Co(b) and Ni(c).

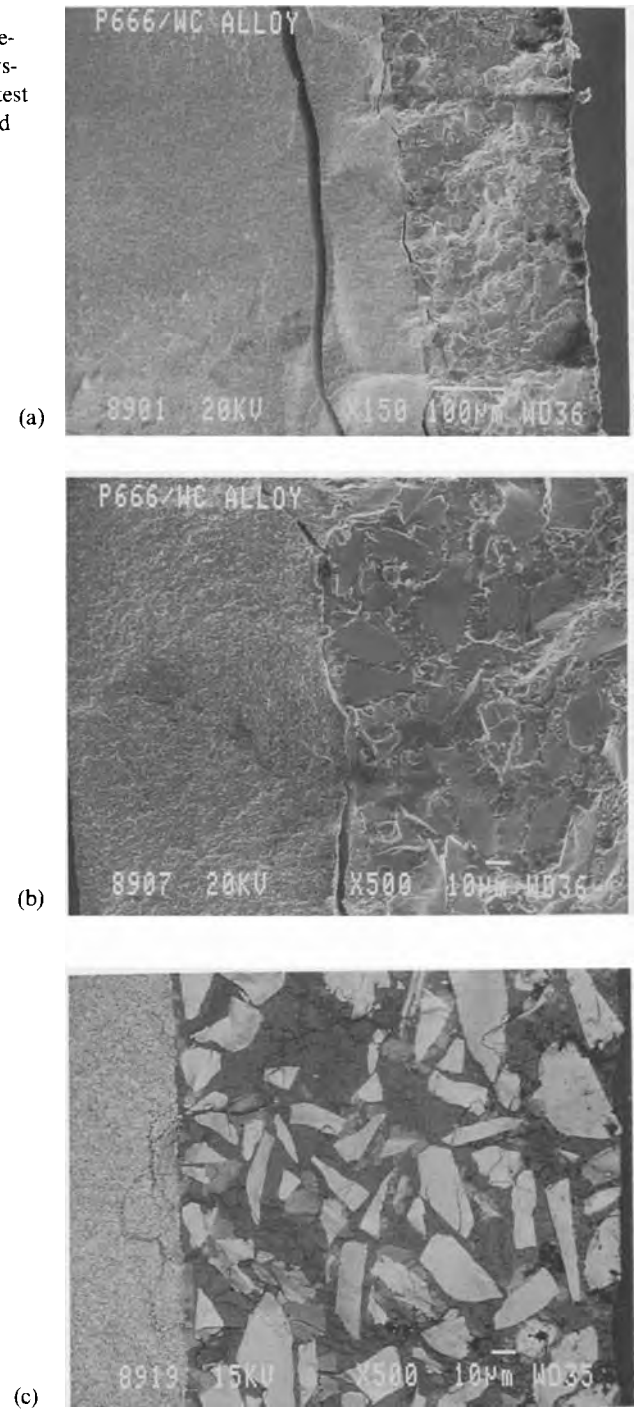

(a)

(b)

(c)

Figure 6-4. Crack behavior of a tungsten carbide-based coating/fine-grained 88WC12NiCo substrate system subjected to a Charpy impact test (a,b) and an electron back-scattered image of the coating (c).

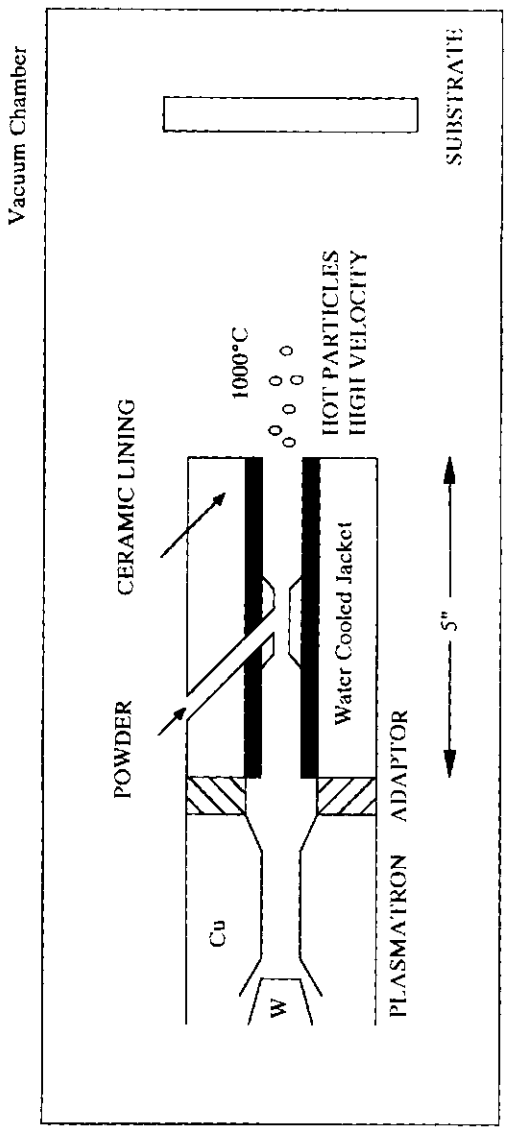

Figure 6-5. Modified plasmatron to reduce decarburization of WC–Co coatings (see text) [26].

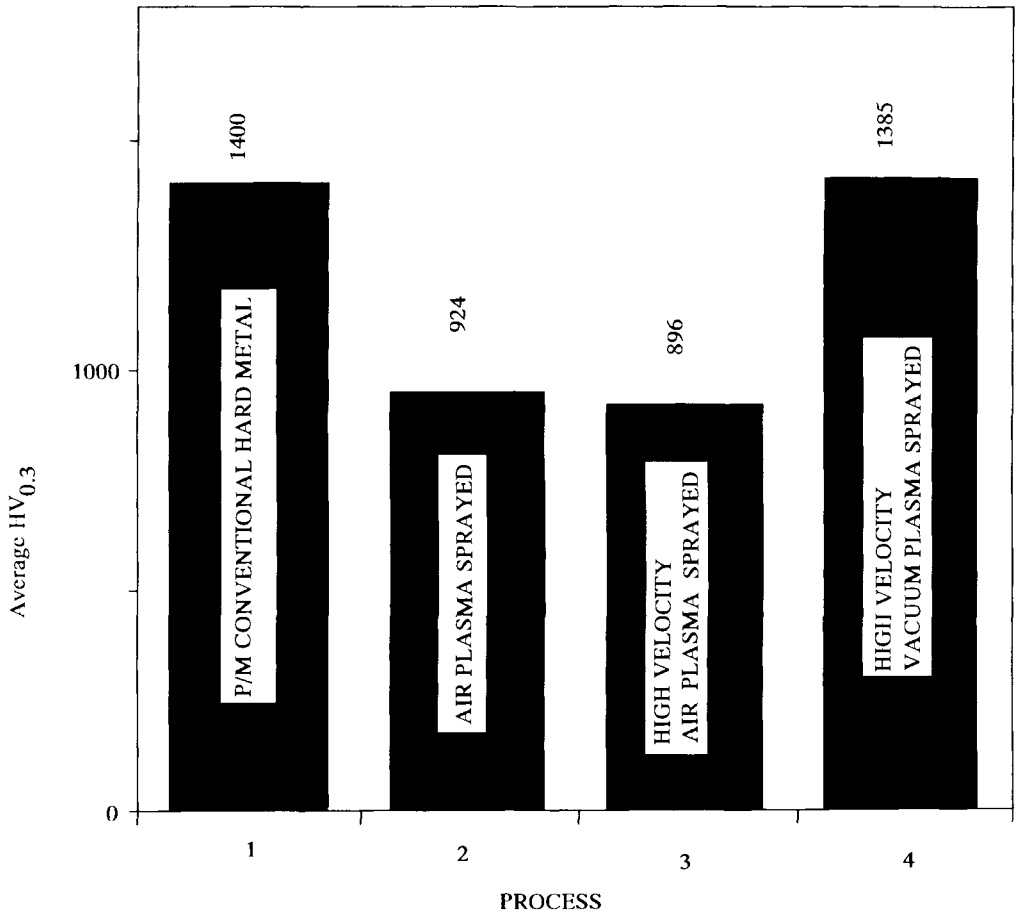

Figure 6-6. Comparison of the microhardness ($HV_{0.3}$) of differently processed 88WC12Co powder (2–4) and powder-metallurgically densified material (1) [26].

6.1.2.2 Titanium Carbide-based Coatings

Under conditions of simultaneous mechanical stress and chemical corrosion, in particular in a steam environment, commercially available WC–Co coatings frequently do not perform well at high working temperatures.

For example, the quest for an increased energy output of power plants and various kinds of heat engines necessitates an increase in the working temperature. In these cases, TiC–Ni is an alternative system [27] that because of higher temperature stability, lower coefficient of thermal expansion, higher hardness and lower specific gravity may outperform other coating systems. If the TiC phase is stable, and well bonded and dispersed in the matrix, a hard, low-friction surface is produced. WC or Cr_xC_y phases tend to decompose at high temperatures thus losing their friction properties.

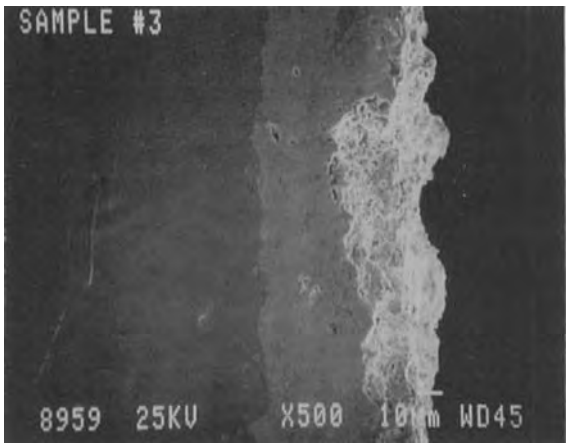

Figure 6-7. Cross-section of a 88WC12Co coating (right) on mild steel (left) [13].

Problems exist, however, in plasma spray operations that result in decarburization of TiC towards TiC_{1-x}. Therefore, TiC has been processed as 'cermet coating clad' in a metal system [28]. In order to suppress decarburization of TiC, a reduction of the dwell time of Ni-plated TiC particles (50TiC50Ni to 30TiC70Ni) utilizing VPS or HVOF techniques led to coatings on mild steel with low porosity (<2%), high microhardness (900–1 000 $HV_{0.2}$ (the subscript refers to the applied load, 0.2 kp)) and high blast erosion resistance (<0.1 $mm^3\ g^{-1}$ at a blast angle of 90°; alumina grit 60 mesh, air pressure 490 kPa) [27]. The VPS coatings outperformed the HVOF coatings also in a reciprocating plane wear test.

The wear properties of TiC-based coatings are a strong function of the powder preparation method. Studies by Mutasim *et al.* [29] showed that a 40% TiC + Ni20Cr powder produced by the PMRS (plasma melted rapidly solidified) method and sprayed with VPS produced a coating with a wear resistance ten times that of a coating of the same composition whose starting powder was produced by physical blending. Similar results were obtained in an earlier study [30]. In this study, a comparison was made of the sliding wear performance of five different hard coatings (TiC reinforced alloys: Resistic CS-40 (45 vol% TiC, stainless steel matrix); Resistic CM (45 vol% TiC, tool steel/Fe,Cr,Mo matrix; Resistic HT-6A (40 vol% TiC, Ni20Cr matrix); 88WC12Co composite powder, and Stellite 6 (Co28Cr4.5W3Fe3Ni1.5Si1Mo1Mn1.15C) sprayed with APS onto steel. The TiC reinforced composite coatings had bond strengths exceeding 58 MPa and sliding wear resistances from 20% higher than the WC/Co coatings, and up to 100% higher than Steelite 6 coatings, depending on the deposit matrix of the TiC reinforced materials (Fig. 6-9a). Also, the type of auxiliary plasma gas (helium or hydrogen) played an important role for the wear resistance of WC/Co and Stellite 6 but did not influence that of the TiC-based coatings. The kinetic coefficient of friction during the sliding wear test was minimized for CS-40 (Fig. 6-9b).

A different way to circumvent the risk of thermal decarburization of TiC under high temperature conditions in a plasma jet is *reactive plasma spraying*. TiC is formed from titanium particles during their flight along the plasma jet. A reactor is

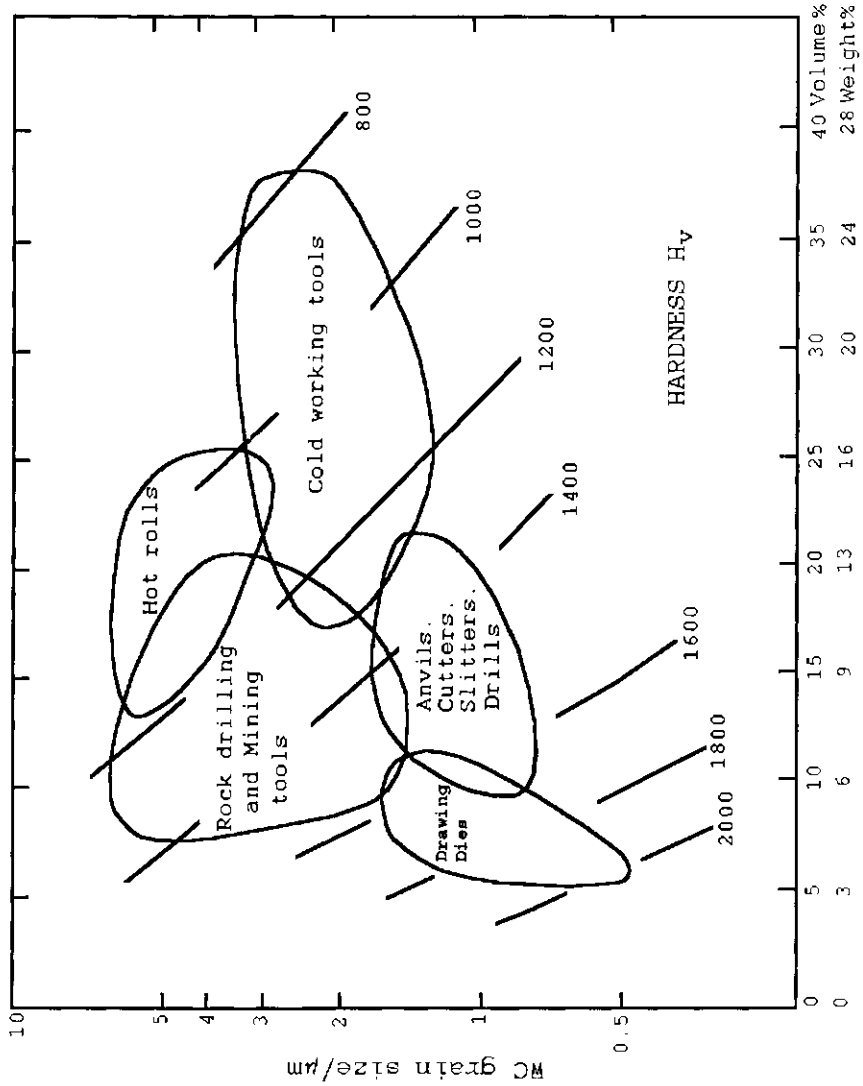

Figure 6-8. Hardness of WC–Co cemented carbide as a function of the WC grain size and the volume content of cobalt. Several application areas are indicated.

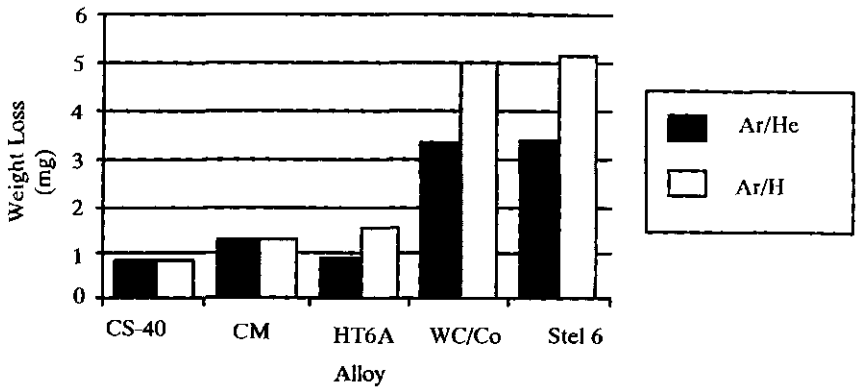

(a)

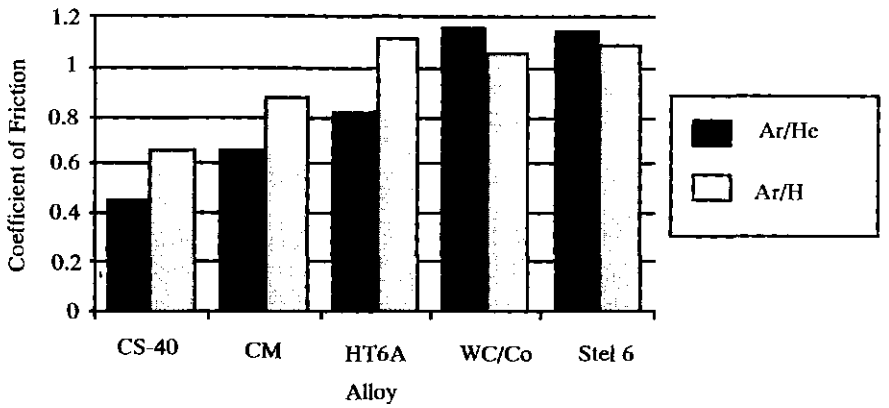

(b)

Figure 6-9. Weight loss (a) and coefficient of friction (b) during sliding wear resistance tests of TiC-metal matrix coatings (CS-40, CM, HT6A alloy). Values for WC/Co and Stellite 6 are given for comparison [30].

added to a conventional d.c. plasmatron into which carbon-containing precursor gases (methane, ethane, propane, acetylene, etc.) are fed (Fig. 6-10). Into the plasmatron titanium powder will be introduced in the conventional manner. Shroud gas (Ar, N_2) led into the reactor tube is thought to prevent build up on the reactor walls of Ti/TiC materials and carbon produced by thermal cracking of the hydrocarbon precursor gases. The modified plasmatron was operated in a controlled, sub-

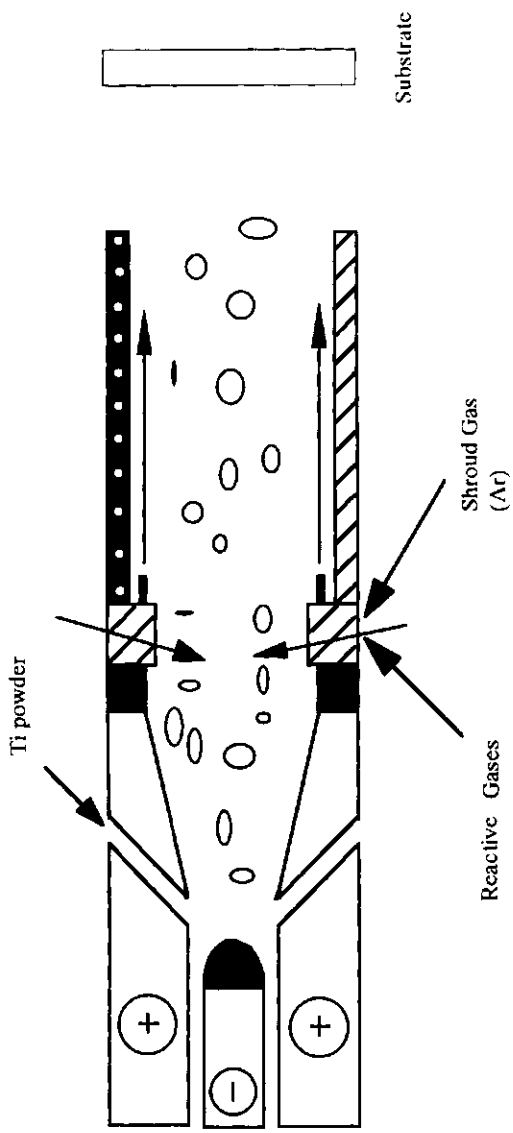

Figure 6-10. Reactive plasma spraying of Ti in a hydrocarbon environment to obtain TiC-containing hard coatings [31].

atmospheric pressure environment. The amount of TiC formed and retained in the coating is a function of several parameters such as substrate temperature, chamber pressure, type of reactive gas, flow rate of the reactive gas, and the method of introduction of the reactive gas [31, 32]. The hard TiC phases were observed predominantly in the intersplat region. The formation and distribution of the hard phases in the coatings suggest a two-stage mechanism illustrated in Fig. 6-11. In these experiments the content of the hard phase is still very low (around 8 vol%) and must be considerably improved by process optimization until reactive plasma spraying of TiC will become an economically competitive technology. A more promising way seems to be to reactively spray Ti/Ni20Cr powder with propylene as a precursor gas [32]. In the coatings, the hard phases Cr_7C_3 and TiC were deposited in very small crystals (<1 μm). From these results it was concluded that reactively plasma-sprayed prealloyed NiCr/TiC powders would show improved wear resistance owing to the better carbide/matrix cohesion of the *in situ* formed carbides Cr_xC_y. Indeed, the reactively sprayed NiCr/TiC material displayed harder coatings (840 $VH_{0.3}$) than nonreactively sprayed prealloyed coatings that showed a microhardness of only 700 $VH_{0.3}$ [33].

Several other papers on TiC-based coatings may be consulted to obtain information on applications and performance optimization [34–37]. The properties of the simple TiC/Ni system can be improved by alloying with other elements, such as molybdenum in the carbide, and cobalt in the binder phase. Preliminary investigations on such (Ti, Mo)C–NiCo coatings sprayed by APS and D-Gun techniques [38] as well as VPS [39] indicate that with proper parameter optimization very hard, highly wear resistant coatings can be produced for a variety of high temperature applications including high temperature erosion protection. It was demonstrated that the typical microstructure of the powders, produced by agglomeration and subsequent sintering, in particular the core (nearly pure TiC)–rim (Ti, Mo)C_{1-x} structure (Fig. 6-12) can be transferred to the coating without significant changes.

6.1.2.3 Chromium Carbide-based Coatings

Although chromium carbide is somewhat softer than tungsten carbide at room temperature (HRC 52 versus HRC 62) it shows excellent sliding-wear resistance [40] as well as superior oxidation and high temperature SPE resistance [41] in a steam environment. It thus offers promising opportunities for protecting steam path surfaces and turbine components from corrosion and erosion [42]. Several attempts have been made in the past to combat corrosion damage, stress corrosion cracking and corrosion fatigue in steam turbines [43] as well as SPE in boilers, tubing and steam lines including superheaters [42]. These attempts include the development of boride diffusion coatings and plasma-sprayed chromium carbide coatings.

The advantage of the *boride diffusion coatings* is that they do not have a line-of-sight limitation (as do plasma spray coatings) but this is more than compensated for by the negative fact that boride coatings can result in a fatigue loss in the ferritic base metal of boiler tubes of as much as 50% [44]. This fatigue loss originates from a combination of lack of coating ductility and the fact that the coating forms a metallurgical bond with the base metal. Strain damage occurs in cyclical thermal loading

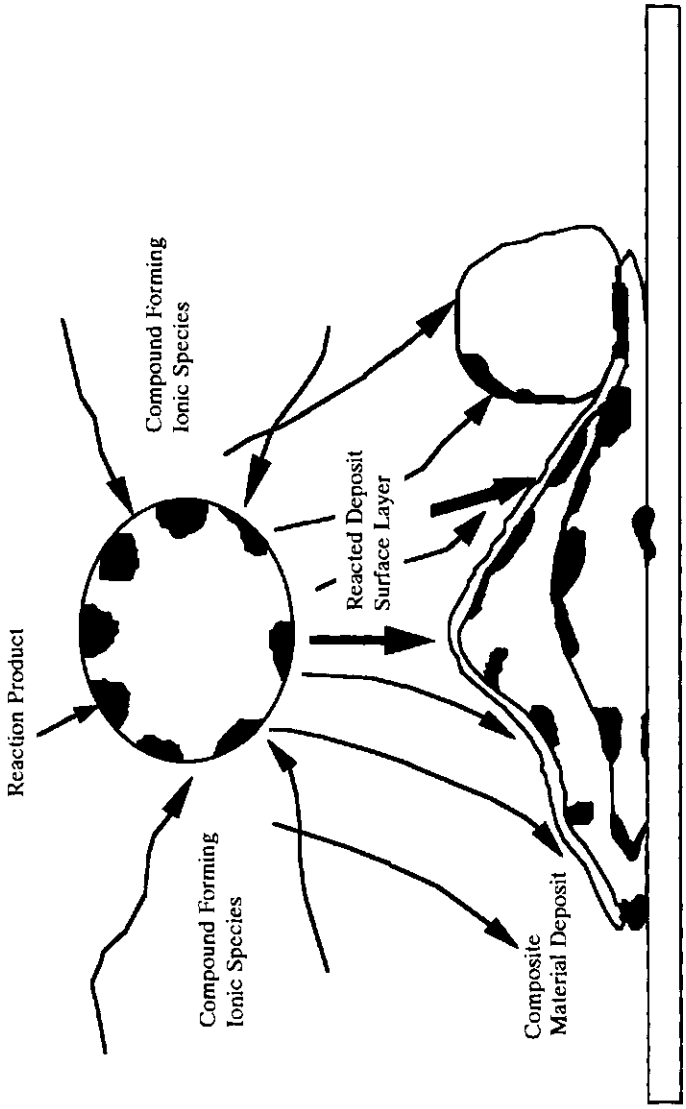

Figure 6-11. Model of TiC formation during reactive plasma spraying of Ti metal powder [31].

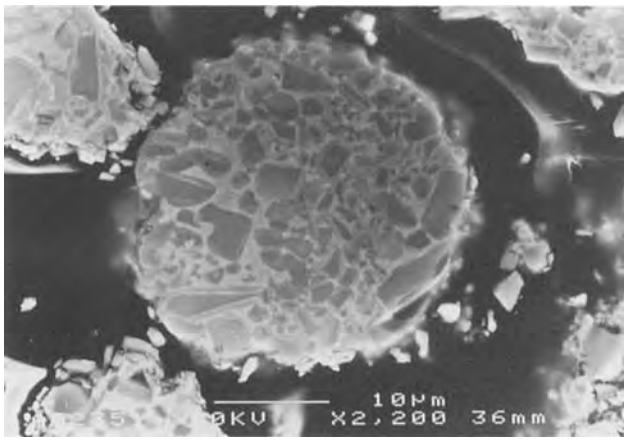

Figure 6-12. Dense as-sintered (Ti, Mo)C–NiCo alloy granule with a typical core (nearly pure TiC)–rim (Ti, Mo)C_{1-x} structure [39].

since the higher Young's modulus of the coating causes it to be put under tension that will be amplified in service and leads finally to cracks perpendicular to the stress direction.

Plasma-sprayed *chromium carbide coatings* can reduce considerably the steam path erosion rate. Comparative erosion tests on chromium carbide sprayed with a D-Gun technique and chromium boride/iron boride diffusion coatings on AISI 403 and AISI 422 martensitic stainless steels showed that at 538 °C the former are clearly superior in terms of SPE with chromite particles (75 μm, 152 m s^{-1}, 30 min) at impingement angles of 30° whereas the latter show higher SPE resistance at impingement angles of 90° [45]. During deposition of plasma-sprayed coatings the heat input into the ferritic base metal is much lower than for boride diffusion coatings. Therefore boride diffusion coatings require a post-coating treatment to restore the strength and ductility to the coated component [42]. The austenitic phase formed at the high diffusion temperature creates internal stresses in the base metal that result in distorsion and thus the need for time-consuming post-coating machining or grinding operations to restore flatness or critical clearances.

Tungsten carbide coatings for the protection against SPE of steam turbine buckets were introduced in the early 1960s by the General Electric company, but it was subsequently found that such coatings have not been consistently effective in preventing erosion damage. Thus new solutions were sought and chromium carbide–NiCr cermet coatings on 12Cr martensitic stainless steel (AISI 422 cast) were developed and tested by the General Electric Turbine Technology Laboratory in a fully-ducted, dynamic burner rig heated by natural gas [46].

The Holdgren practice [42] used for protection of steam path surfaces is similar to coating practices specified by General Electric, and the Pratt & Whitney company for rotating aircraft components. An exothermic nickel aluminide bond coat, consisting of spherical aluminum powder particles overcoated with shells of nickel, is applied to the base metal. During spraying the two elements react to form a nickel aluminide intermetallic compound. Since this reaction results in the evolution of heat

that under optimum spraying conditions continues after impact and coating formation, microdiffusion may occur between base metal and bond coat thereby enhancing the adhesion strength by a factor of two compared to NiCr bond coats.

The reason for the outstanding erosion resistance of chromium carbide coatings seems to be based on precipitation-strengthening of Cr_3C_2 by the formation of Cr_7C_3 due to decarburization (oxidation) of the former (secondary carbide precipitation) [47]. The as-sprayed, carbon-deficient Cr_3C_2 transforms in service to Cr_7C_3, thereby more than doubling the hardness and greatly enhancing the SPE resistance [48]. Since this precipitation-strengthening mechanism requires an air atmosphere, good erosion resistance is promoted by APS rather than VPS. Also, fine chromium carbide powders and pre-aging to optimum hardness further increases SPE resistance, as does the replacement of the NiCr or NiCrMo matrix by FeCrAlY or CoCrNiW [48]. Alloys such as FeCrAlY have also been tested in their own right as a barrier layer to high temperature erosion on coal combustion and conversion processes including fireside erosion, erosion of steam turbines and corrosion-assisted wear in flue gas desulfurization equipment [49]. The protection mechanism is based on the formation of Al_2O_3 scale [50].

Another widespread and yet unsolved problem exists in the petrochemical industry. High temperature steam cracking of ethane to produce ethylene causes several deleterious effects in the steel tubing in the convectively and radiantly heated sections of a typical cracking furnace. These effects include external oxidation and internal oxidation/deposition of coke that is thought to be formed under the catalytical action of nickel oxide. This oxide is formed from oxidation of nickel as an alloying element for steel (AISI 304, AISI 410) or nickel superalloys (Inconel 800, Hastelloy X) added to impart high temperature resistance. The coke deposited on the internal surfaces of tubing tends to form carbides with other alloying metals in the steel that can migrate into the metal. As a result, blistering and cracking of the steel can occur. Also, reduction of the heat conduction capability of the tubing may lead to local overheating in the convection section of an ethylene steam cracker. Since the surface roughness of the internal tubing walls seem to promote the rate of coke deposition [51, 52] mechanical polishing or application of a smooth coating can reduce the coke layer formed. Also, introduction of trace amounts of sulfur compounds or antifoulants into the process gas stream inhibits the catalytic effect of the metal surface and may offer some moderate measure of protection [53]. Finally, metallurgical remedies tested were either related to higher alloyed steels to reduce the carbon gradient or to the introduction into the metal of carbide-stabilizing additions such as W, Mo, Nb, or V. Unfortunately, these metal additions have adverse effects on the high temperature oxidation resistance and their oxides may form low melting eutectics with nickel or chromium oxide.

In order to reconcile the material requirements with the severity of the environmental attack, functional chemical barrier coatings (CBC) must be developed with the following properties:

- high temperature resistance,
- high corrosion resistance,

- chemical inertness,
- high hardness,
- high wear, abrasion and erosion resistance,
- creep resistance,
- good adhesion,
- high fracture toughness,
- good thermal conductivity,
- thermal shock resistance,
- smooth surface/low porosity, and
- thermal fatigue cracking resistance.

The first five criteria are best met by ceramic coatings, the remaining seven by metal or alloy coatings. To develop a coating material that would meet all requirements, ideally a type of coating should be selected that combines synergistically the advantages of both material classes. This, however, is extremely difficult to achieve since many of the desired properties listed above are noncompatible or even mutually exclusive. For example, partially stabilized zirconia (PSZ) would have all the advantages of ceramic coatings including good adhesion but would fail to meet the important criteria of good thermal conductivity and low porosity. In general, the most difficult problem is to match the coefficients of thermal expansion and the thermal conductivities of the coating and the metal substrate. Therefore, the composite coating performance will always have to be compromised. Attempts have been made to plasma-spray composite chromium carbide-based coatings such as $62Cr_3C_225W_2C5TiC4Ni3Mo1Cr$ that show excellent erosion resistance in a high temperature steam environment. While there seems to be controversy about the role chromium is playing as a possible catalyst for coke formation, there also exists evidence that increasing the chromium content and decreasing the nickel content of the alloy metal reduces the coke deposition rate [54]. There is, however, no general solution available yet to the problem of coke deposition, and chromium carbide coatings may be but a small step towards such an approach.

6.1.2.4 Boride-based Coatings

Although the borides and diborides of the transition metals of the fourth to sixth group of the periodic table have a metallic character (Fig. 8-1), extreme hardness, high melting points and high chemical stability they are difficult to process in plasma spray operations [55]. Early attempts to develop boride coatings used the deposition of CrB_2 from a Cr–B–Si–Ni alloy by a welding torch [56]. Modern approaches rely on the so-called 'auxiliary metal bath process' (Menstruum process) [55, 57] that promotes the reaction of elements by dissolving them in a liquid metal. To deposit TiB_2, a ferrotitanium alloy is reacted with elemental boron in an iron bath according to:

$$a\{FeTi\} + b\{Ti\} + c\{B\} = d\{TiB_2\} + e\{Fe\}. \qquad (6\text{-}1)$$

Also, the synthesis route can start with melting ferrotitanium and ferroboron mixtures in an iron auxiliary bath [58] according to:

$$e\{Fe\} + f\{FeTi\} : \{B\}/\{Ti\} < 2 \tag{6-2a}$$

$$a\{FeTi\} + b\{Ti\} + c\{FeB\} \rightarrow d\{Fe\} : \{B\}/\{Ti\} = 2 \tag{6-2b}$$

$$h\{Fe\} + i\{Fe_2B\} : \{B\}/\{Ti\} > 2 \tag{6-2c}$$

Obviously, the synthesized product depends on the $\{B\}/\{Ti\}$ atomic ratio and on the temperature. In the case of Eq. (6-2a) the reaction product contains Fe and FeTi compounds, in the case of Eq. (6-2c), Fe and Fe_2B occur. Only when the $\{B\}/\{Ti\}$ ratio is 2, the reaction product consists of titanium diboride in an iron matrix. Thus it is possible to produce such coatings by plasma spraying micropellets of ferrotitanium and ferroboron. These micropellets may act as 'microbath' in which the TiB_2 synthesis takes place. It should be emphasized that this technique mimics the commercial electrolytic production of borides in a bath of fused borax with highly concentrated boron depositing along the cathode at 900 °C. With additional metal oxides present in the bath, metal borides are deposited in well crystallized agglomerates by reaction of the boron with the reduced metals (Eq. (6-1)) [3].

6.1.3 Oxide Coatings

As frequently pointed out in the preceding sections, cemented carbides do not stand up well to chemical degradation at high temperature, in particular a steam environment, due to decarburization, oxidation and matrix-alloying under formation of η-carbides. In these cases the material of choice may be an oxide ceramic coating, most frequently alumina and chromia, and their modifications and composite materials. However, the advantage of considerable increase in chemical and thermal resistance is counterbalanced by the disadvantage of generally low values of the coefficient of thermal expansions, thermal conductivity, mechanical strength, and fracture toughness. Also, the adhesion of such oxide coatings to a metallic substrate is compromized by the non-metallic bonding character of oxides. Indeed, their high proportion of ionic bonds (see Fig. 8-1) prevent the formation of compatible lattice planes at the interface. In such a case, thin mediating transition layers, for example TiC (see Fig. 8-2) may be useful. As will be shown later (Sec. 6.2), thermal barrier coatings of stabilized zirconia require metallic alloy bond coats to alleviate the gradient in the coefficients of thermal expansion between metal substrate and ceramic oxide coating. On exceeding a limiting coating thickness the residual tensile stresses built up in the coating layer will exceed the yield strength of the ceramic material, and delamination and catastrophic cracking will occur (see Sec. 5.5.5, Fig. 5-20b). Therefore, careful control of the residual tensile stresses in ceramic coatings by application of an appropriate bond coat, well-designed temperature schedule including substrate preheating, or reinforcing measures by addition of other oxides [59] is mandatory for

oxide coatings that are supposed to stand up to the severe in-service conditions in a high-temperature corrosive environment.

6.1.3.1 Alumina-based Coatings

During plasma spraying, alumina transforms from its α-modification, stable at room temperature, to the γ-modification with a defect spinel lattice. Thus plasma-sprayed alumina coatings contain substantial amounts of the essentially metastable γ-phase. The ratio α/γ can be used to characterize the degree of melting of the starting powder with the assumption that high amounts of residual α-phase signal incomplete melting. Also, high amounts of γ-phase seem to lower the wear resistance of alumina coatings even though the microhardness is apparently little affected [21].

Due to its hardness and good electrical insulation, plasma-sprayed alumina coatings are being used as top coats for insulated metal substrates in automotive applications as about 50 μm-thick coatings for aluminum heat-sinks. On these top coats electronic circuitry is then built up. A basic requirement for this application is a maximum dielectric breakdown strength in the range of several hundred volts per 25 μm [60]. This, however, is compromized by the formation of the γ-phase that tends to absorb water [61] that will have a significant effect on the dielectric properties of the coating.

In many cases alumina is used in conjunction with titania: increasing TiO_2 content increases coating fracture toughness but reduces hardness and friction coefficient thus leading to decreased wear resistance. A compromise is to use a ceramic material that contains only a small amount of titania. Alumina/titania (97/3) coatings (called 'grey alumina') are used, for example, to prevent wear, cavitation erosion, and chemical corrosion of plungers from reciprocating and centrifugal pumps [62]. Such coatings are known to be very dense, and produce the smoothest surface of any as-sprayed ceramic coatings. This reduces the amount of post-spray grinding and polishing treatment required. The coatings must be thin to conform to available clearances between plunger and barrel of the pump. On the other hand, they should be hard (70–80 HRC) and show high adhesion strength (>50 MPa). Figure 6-13 shows the cross-section of a thick alumina/titania (97/3) APS coating on a commercial-grade, hot-rolled sheet steel (A 569). The coating appears to be very dense since the apparent porosity is mostly related to grain plug-out during preparation of microscopic samples. Two systems of cracks appear that are due to, first, residual tensile stresses owing to the exceptionally thick (0.9 mm) coating (horizontal cracks) and, second, delamination (vertical cracks). The microhardness of such coatings depends on the thickness and obeys a linear law, $HV_{0.3} = ad + b$ [MPa] with $a = 12$ MPa, d = coating thickness in mm, and $b = 97.4$. Abrasion wear test mass losses (ASTM G65) of the coatings show an inverse proportionality to the thickness ($\Delta m = c/d$ [mg], with $c = 45.3\ \mathrm{mg\,mm^{-1}}$ and d = coating thickness in mm) and to the microhardness ($\Delta m = A\,HV_{0.3}^{-B}$ [kg], with $A = 4.3 \times 10^{24}$, $HV_{0.3}$ = microhardness in $\mathrm{kg\,mm^{-2}}$, and $B = 9.5$ (Fig. 8-15). Similarly dense coatings with SPE-resistance approaching that of bulk alumina were produced by Kingswell *et al.* [63] and Chon *et al.* [64].

To further reduce porosity of alumina-based coatings to below about 5%, laser-

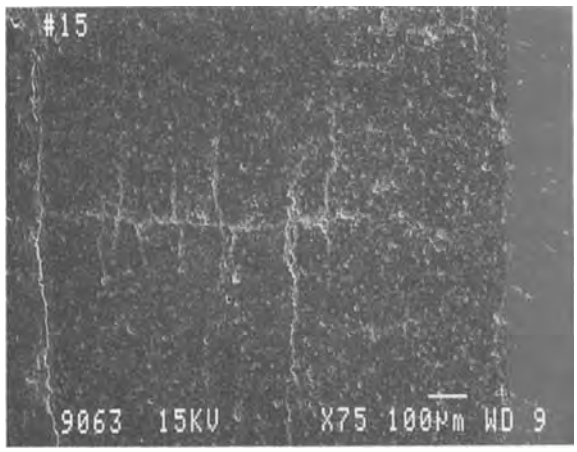

Figure 6-13. Dense Al_2O_3/TiO_2 (97/3) APS coating on A 569 steel (left) [62].

glazing can be used to densify to topmost layer of the coating and thus to seal it against penetration of corrosive agents. Inevitably the ceramic layer shows creasing or even severe cracking due to the induced thermal stresses when subjected to a high-power laser beam. These cracks frequently not only propagate through the laser-melted top layer but further extend into the underlaying material. A solution to the severe cracking problem may be to introduce into the laser beam ceramic compositions with lower melting points that would develop smaller solidification stresses and less differential strains with respect to the unheated alumina material. Such attempts have been made by selecting Al_2O_3/TiO_2 (60/40) that transforms on laser-melting to a mixture of Al_2TiO_5, TiO_2 and α-Al_2O_3 [65], and Al_2O_3/ZrO_2 [66]. In both cases the cracking could be considerably reduced.

An instructive example is the optimization of WC/Co-tipped saw teeth for rip-sawing wood in the unseasoned state as performed in sawmilling operations. These saw tips were CVD-coated with Al_2O_3–TiO_2 to obtain self-sharpening characteristics of the tool [67]. This requires that the abrasive and erosive/corrosive wear resistance of the coating be synchronized with the wear resistance and microstructure of the substrate so that a cutting edge can be produced that maintains a sharply pointed profile, i.e. that is self-sharpening. As shown in Fig. 6-14 this is achieved by coating 60WC40Co tips (E) with alumina/titania on the rake face (rake angle 30°, clearance angle 7°). This materials system maintains a reasonable cutting edge during most of the cutting period for up to 60 km of cutting path since the wear-induced retreat of the surface of the coating and that of the substrate roughly coincide. The species cut was unseasoned Western Red Cedar (*Thuja plicata* Donn) of British Columbia, Canada, and the numbers next to the wear profiles indicate km of cutting path. At this point, a self-sharpening behavior up to 60 km is not sufficient for industrial application that require a mininum cutting path of 200 km between mechanical sharpening operations. This approach will become economically competitive to current technology only if a modified substrate material could be designed that ensures such high cutting paths.

Recently, alumina and alumina/zirconia (4:1) coatings have been used for oxida-

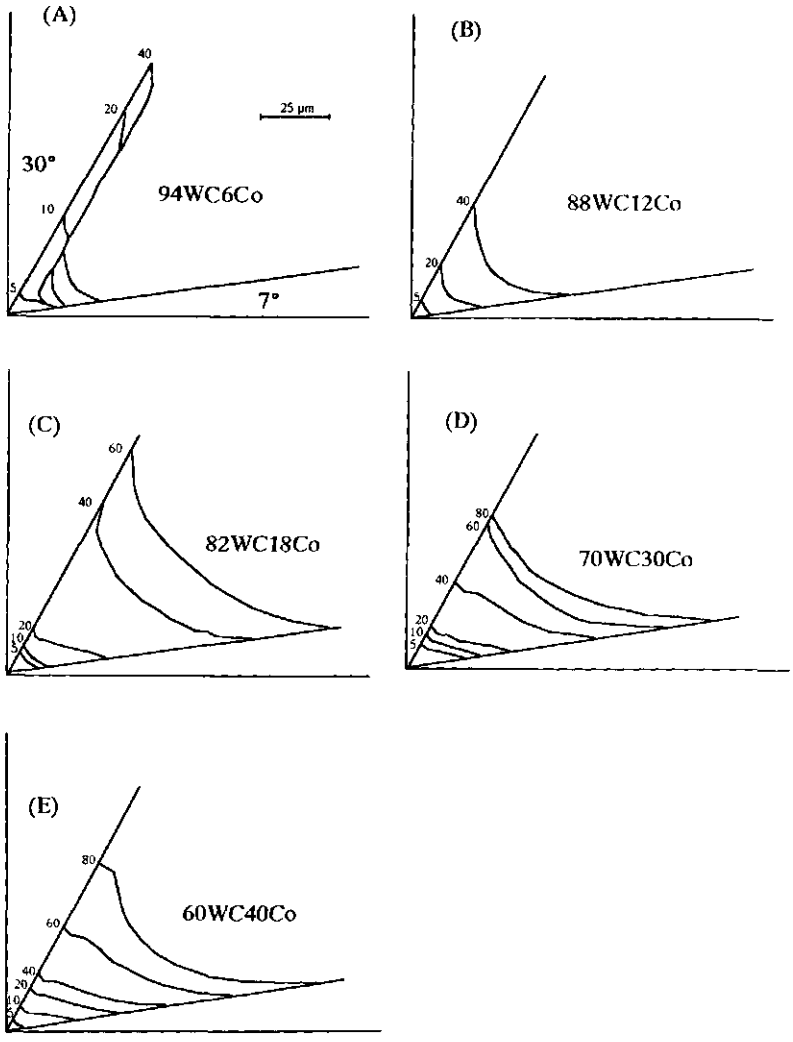

Figure 6-14. Self-sharpening wear behavior of WC-Co-tipped saw teeth coated with alumina/titania. The numbers refer to kilometers of cutting path [67].

tion protection of RSiC kiln aids used in fast firing of China ware. Vacuum plasma-sprayed alumina/zirconia coatings of 400 µm thickness performed best: the RSiC material showed an SiO_2 content of less than 2% after exposure to an O_2/N_2 (1:1) gas mixture for 2 500 h [68].

6.1.3.2 Chromia-based Coatings

Chromia coatings are being applied when corrosion resistance is required in addition to abrasion resistance, i.e. in the case of strongly synergistic corrabrasion. Such

coatings adhere very well to most metal substrate surfaces and show exceptional hardness of 2 300 $HV_{0.05}$ [69]. Applications abound in chemical industry as coatings of joints in movable parts, in water pumps, steel rollers for ore classification, and smooth top coats for printing rolls [70]. Chromia coatings are also gas tight as shown by the occurence of protective oxide films against sulfidation and carburization on high chromium steel and alloys at high temperatures [71]. While during APS operations only the di-trigonal α-modification (corundum structure) occurs, at reduced pressure Cr_2O_3 decomposes forming metallic chromium as well as a metastable Cr_3O_4 phase [69].

Chromia coatings perform particularly well in ship and stationary diesel engines where a corrosive environment is created by the use of less expensive but lower quality diesel fuel [72]. Serious corrosion occurs through the impurities of the fuel such as sulfur, vanadium, sodium, etc. Erosion is also of concern because catalytic cracking of fuel precursors introduces Al_2O_3–SiO_2 particles into the diesel fuel. Thus chromia coatings are required, for example to protect valve stems of diesel engines from wear and corrosion. Such coatings must be optimized for good adherence (>40 MPa) and maximum fracture toughness. Better coating quality can be obtained by HVOF spraying [73]. Here microhardnesses can be routinely achieved exceeding 2 000 HV and a porosity of less than 1%.

Friction coatings on braking units of transportation machines have been suggested that consist of plasma-sprayed 60%Cr_2O_3 + 40%TiO_2 coatings with a very high friction coefficient of 0.8 and a porosity <3.5% [74].

6.1.4 Metallic Coatings

Metallic coatings are, in general, easy to apply to other base metal surfaces by a variety of thermal spray techniques, usually flame- and HVOF-spraying. However, refractory metals with very high melting points such as W, Mo, Ti, Cr, Nb, or Ta, and superalloys such as Inconel, Hastelloy and NiCoCrAlY-type alloys require APS- or VPS-plasma spray techniques.

6.1.4.1 Refractory Metal Coatings

Problems with Mo and W wear- and corrosion-resistant coatings occur because of the pronounced tendency of the molten metals to absorb gases during the spraying process [58]. For example, liquid molybdenum exposed to air at about 2730 °C absorbs approximately 13 wt.% oxygen [75]. Oxygen will be entrained from the surrounding air into a turbulent argon plasma jet and will react with the molten Mo particles forming MoO_2 that segregates during solidification along the grain boundaries of the splats. Thus VPS technology has been used to deposit Mo and W coatings [76–80]. Mo coatings show very good adhesion to steel substrates presumably due to the formation of a thin metallurgically bonded Fe–Mo alloy at very high contact temperatures [81]. However, with proper spray parameter optimization using statistical experimental design methodology it appears to be feasible to use APS technology [82] (see Sec. 8.4.2).

Nb/Hf and Ta plasma-sprayed coatings are being applied by VPS technology to the interior surface of advanced gun barrels because of their high temperature strength, creep resistance and toughness [83]. Addition of 15 vol% TiC increased the ultimate tensile strength (UTS) of 89Nb10Hf1Ti alloy from 469 MPa for the nonreinforced material to 523 MPa at room temperature. However, addition of 45 vol% TiC to 90Ta10W reduced the UTS from 606 MPa for the nonreinforced material to 284 MPa at room temperature. The UTS values at 1093 °C (2000 °F) were 209 MPa (89Nb10Hf1Ti) and 197 MPa (89Nb10Hf1Ti + 15 vol% TiC) and 191 MPa (90Ta10W) and 156 MPa (90Ta10W + 45 vol% TiC), respectively.

Ti and Ta plasma-sprayed coatings require VPS technology since at high temperatures considerable amounts of oxygen and nitrogen can be interstitially absorbed that compromize the properties of the coatings [84, 85]. With VPS, dense (<1% porosity), well adhering (72 MPa for 92.5Ti5Al2.5Fe) titanium coatings could be produced [85].

Cr- and Cr-based coatings are used to protect waterwall tubes in boilers in paper, power, and chemical process industries. Plasma-sprayed high chromium–nickel–titanium alloy (TAFALOY 45CT) coatings were developed to combat degradation by chemical corrosion and erosion of unprotected waterwall tubes made from carbon steel in steam generating boilers [86]. Thick Cr coatings on copper substrates were developed as PVD sputter targets [87].

6.1.4.2 Superalloy Coatings

So-called superalloys are nickel-based γ'-phase precipitation hardened alloys of nickel aluminide, 'NiCoCrAlY' alloys and even more complex high-nickel alloys with additions of Cr, Co, Mo, W, Ti, Nb, B, Zr, and C [88]. They show excellent high temperature-corrosion resistance, and are predominantly applied to gas turbine engine blades and vanes. One of the main advantages of such overlay coatings is their inherent compositional flexibility that permits tailoring of the coating composition for both oxidation resistance and coating substrate compatibility [89]. This compositional flexibility allows the addition of active elements such as yttrium that improves the adherence of the oxide scale during in-service thermal cycling [90]. Currently, two competing techniques are used for applying NiCoCrAlY overlay coatings: electron-beam physical vapor deposition (EB–PVD) and low-pressure plasma spraying (LPPS, VPS). Increasingly, plasma-spraying becomes economically more attractive owing to advantages such as lower cost, tighter compositional control, and greater process flexibility.

One of the most important properties to be optimized is the low cycle fatigue (LCF) [91], and stress rupture and creep [92] behavior of plasma-sprayed NiCoCrAlY coatings. The coatings can significantly affect the mechanical superalloy component, for example oriented single-crystalline PWA 1460. The higher ductility of the coating compared to the diffusion aluminide coatings (see Fig. 1-5) is beneficial to the thermomechanical fatigue life of the coated superalloy component. However, at higher temperature the coatings are significantly weaker than the superalloy substrate and are thus considered to be non-load-bearing [92]. The LCF and creep

behavior is essentially connected with the complex microstructure of plasma-sprayed overlay coatings. The fine grained two-phase microstructure consists of a NiAl-phase (β) and a Ni-rich solid solution (γ). This γ-phase contains extremely fine-grained Ni_3Al (γ′) precipitates [93]. A recent study [94] dealt with the precipitation and transformation kinetics of the structurally reinforcing γ′-phase. According to this transmission electron microscopy work, in an as-sprayed coating γ′- and β-phase were detected whereby the spherical γ′-phase was surrounded by β-phase. It was therefore concluded that the γ′-phase crystallized primarily from the liquid, and subsequently the β-phase during solidification of the plasma-sprayed splats. During heat treatment at 1273 K for 4 h to homogenize the coating, most of the γ′-phase was transformed into γ-phase by solid state diffusion of Co and Cr from the β- to the γ′-phase. This results in a decrease in microhardness and low cycle fatigue strength. In aged coatings at 873 and 973 K the γ′-phase was reformed and α-Co precipitates were observed in the β-phase. The reverse diffusion of Co to the β-phase from the γ-phase might contribute to ordering transition from the γ-phase to the γ′-phase. This is accompanied by a hardening process of the aged coating. In conclusion, to retain the hardness, and LCF and creep resistance of the NiCoCrAlY coatings in service, elements should be added that stabilize the γ′-phase such as Ti, V, W, Ta, or Mo. This sequence explains the observations by Gayda *et al.* [91] that NiCoCrAlY coatings show significant softening in LCF runs at 650 °C but show improved fatigue life and cyclic hardening at 1050 °C that may be related to a slower transgranular crack growth rate due to precipitation-hardening by the reformed γ′-phase.

In addition to LCF- and creep-resistant coatings NiCoCrAlY is also being used extensively as a bond coat or graded intermediate layer for partially-stabilized zirconia (PSZ) thermal barrier top coatings (TBCs) (see 6.2). In these applications it has a two-fold function. First, it provides a gradient of the coefficient of thermal expansion (CTE), i.e. it bridges the gap between the CTE of the Inconel or Hastelloy superalloy structure and that of the PSZ. Secondly, it protects the superalloy from hot corrosive gases penetrating the porous PSZ coating.

6.1.5 Diamond Coatings

The overwhelming majority of industrial thin diamond films and coatings is being produced by CVD, plasma-assisted CVD (PA-CVD), ion beam deposition, and eximer laser ablation techniques [95, 96]. Work in this area is directed towards electronic high-temperature devices, high-power switches, blue light-emitting diodes, radiation-hardened electronics, and ultra-wear-resistant overlays. While qualitatively superior diamond films could be grown with these well-established techniques, their pityfully low deposition rates of the order of only a few μm per h precluded any large scale industrial applications. This changed with the invention of a d.c. plasma jet process (DIA-JET) by Fujitsu Laboratories [97]. The method relies on argon as a plasma gas, and a reactive mixture of 5–20 l min^{-1} of hydrogen and 0.01–0.2 l min^{-1} of methane. Deposition rates were as high as 0.25 mm h^{-1}, and values exceeding 1 mm h^{-1} have been reported [96]. The short distance between nozzle and substrate

(<20 mm) requires very effective cooling of the substrate since temperatures exceeding 1300 °C lead to graphite deposition. Here lies one of the major shortcomings of the technique: the high substrate temperature does not allow for the use of steel since instead of diamond carbides will be deposited. This limitation can be somewhat overcome by an intermediate inert molybdenum or tungsten bond coat. However, diamond films on tungsten-coated steel show rather weak adhesion strength [98]. While silicon, alumina and vitreous silica substrate have been coated in the past [99], modern work was concerned with developing ultra wear-resistant coatings for WC/Co [98, 100, 101] and silicon nitride cutting tools [101] and silicon carbide ceramics [102].

At relatively high methane concentrations the polycrystalline diamond coatings show cube-shaped crystals whereas low methane concentrations show octahedral crystals. The crystal morphology is also a function of the deposition temperature: {111} morphology is typical for low substrate temperatures (700 °C), {100} morphology appears at higher temperatures (1100 °C) [103].

The mechanism behind the process is still somewhat elusive. It is thought that the source gas dissociates in the high temperature plasma jet and forms activated atoms, ions and radicals such as H, CH, C_2H^*, CH_3^+, or CH_3^*. Thermodynamic self-cooling occurs in the plasma jet when it exits the nozzle at very high speed. This process is augmented by entrainment of eddies of external cold gas that break up the potential core of the plasma jet, thereby shifting the initially laminar into a turbulent flow regime (Fig. 3-29). This will further reduce the mean temperature and, to a certain extent, the velocity of the jet. Thus the plasma enters a nonequilibrium state with an abundance of activated radicals remaining in the jet which transports them quickly to the substrate surface before they can recombine.

Figure 6-15 shows a typical setup of a d.c. plasma jet-CVD process [98]. With such an apparatus optimized fine-grained diamond coatings could be produced with a high deposition rate at a substrate temperature of about 1000 °C, chamber pressure of 300 mbar, CH_4/H_2 ratios of less than 5%, and stand-off distance of 70 mm. Best results in terms of coating density were reached with surface roughness values of 0.25 µm [100].

Quick and easy production of medium quality diamond films has been reported using a simple oxyacetylene welding torch [104, 105] in which acetylene provides both the carbon source and a high hydrogen flux. Calculations of the sticking probability of various species occuring in a thermal plasma, fed by methane and hydrogen, showed that gas-phase precursors to diamond are acetylene or acetylene-like radicals [106]. A sticking probability of 10^{-3} for acetylene gives calculated growth rates that compare favorably with experimental growth rates found by Kurihara *et al.* [97] and Matsumoto [103]. Acetylene-like radicals provide for much increased diamond growth rates in d.c. plasma jet deposition but for poorer quality films [107] compared with CH_3 radicals whose gas phase concentration is thought to be the rate-determining step in a typical slow CVD process. On the other hand there is a suggestion that the high growth rates in a d.c. plasma jet are related to high gas phase temperatures. Diamond growth species, whatever their nature might be, may be very effectively produced in 'hot spots', and subsequently rapidly quenched to temperatures below 1 000 °C on the substrate.

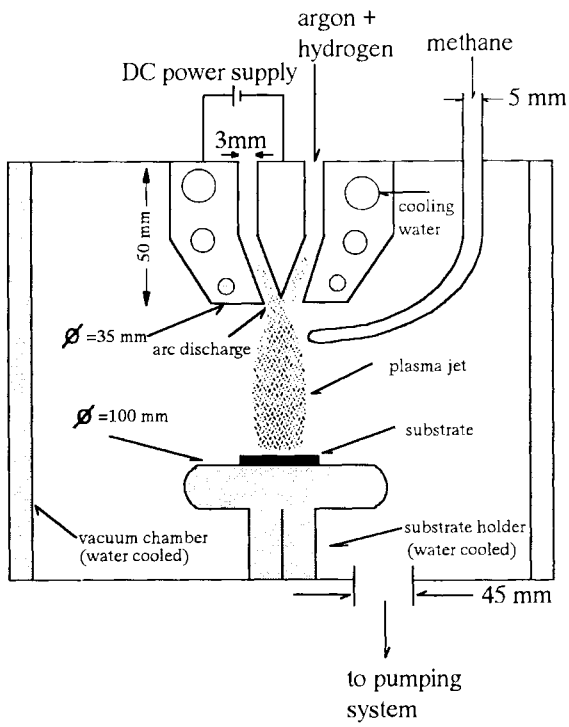

Figure 6-15. Typical setup of a d.c. plasma jet-CVD reactor to deposit diamond films [98].

6.2 Thermal and Chemical Barrier Coatings

6.2.1 Yttria-Partially Stabilized Zirconia Coatings (Y-PSZ)

Development and improvement of thermal barrier coatings based on partially-stabilized zirconia (PSZ) are carried on in two main areas.

The first area relates to the aerospace industry and is concerned with coating of austenitic superalloy blades and vanes of gas turbine engines, combustor cans and turbine shrouds. These efforts provide an excellent example of the sophistication now reached by ceramic coatings. Such coatings increase the lifetime of components subjected to a variety of degrading processes. As shown in Fig. 6-16, the lifetime of an uncoated superalloy turbine component part is limited by mechanical fatigue at temperatures below 800 °C, by hot corrosion between 800 and 900 °C, and by thermal fatigue between 900 and 1 050 °C. Above that temperature, oxidation and creep are life controlling [108]. Thermal barrier coatings fulfill a vital function by increasing turbine blade cooling efficiency, and in conjuction with MCrAlY (M = Ni, Co, Fe) (see Sec. 6.1.4.2) bond coats, prevent hot corrosion of the superalloy by molten salts and corrosive gases. It is thus said that a modern jetliner would not make a single transatlantic flight, but for the coatings [109].

The second area of application is as a potential material for inclusion in recip-

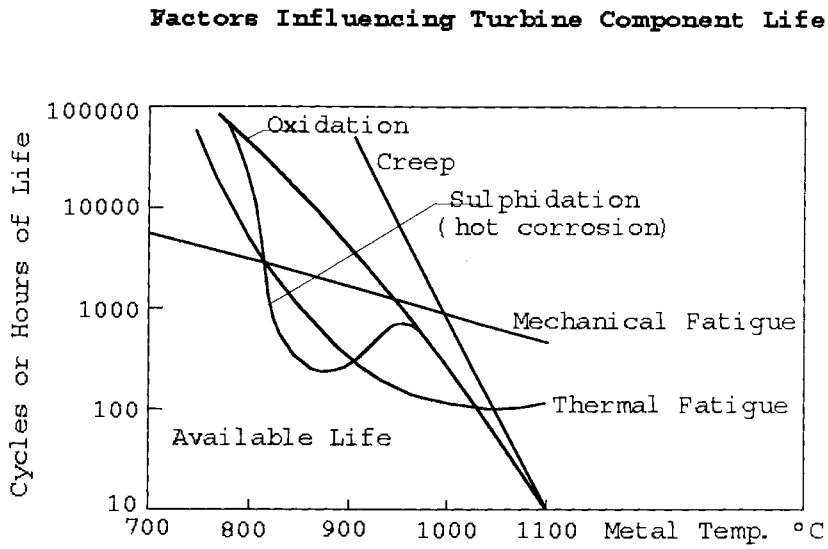

Figure 6-16. Factors influencing the lifetime of gas turbine components [108].

rocating internal combustion engines, principally diesel engines. The goals are to insulate components such as pistons, valves, intake and exhaust ports, and to protect moving parts from wear and corrosion. The quest for increasing fuel economy and decreasing levels of hydrocarbons in exhaust gases necessitates an increase in combustion temperatures. Recently, a joint venture between Adiabatic Inc, and the USA army has been carried out to develop thick TBCs and other ceramic wear coatings for a military adiabatic diesel engine. The thick (0.75 mm) zirconia-based TBC (called 'TTBC') was applied to the recess in the combustion face, to the intake and exhaust ports, and to the piston combustion bowl. The intermediate piston rings were coated with alumina–titania wear ceramic, and the cylinder liner with a proprietary tribological coating. Fuel economiy improved from 16 to 37%, and the engine has survived a 400 h durability test with very low lubricating oil consumption.

Currently 90% of produced zirconia precursor powders are used for gas turbine applications, but this market segment is estimated to decrease to 40% by the year 2000, whereas diesel engine applications will increase from todays 2% to 40% at the turn of the century [99]. Figure 6-17 shows a NASA scenario of development trends in in-service temperatures of gas turbines for aerospace applications. The first step in the development cycle has been already reached by incresing the turbine blade surface temperatures to 1 100 °C. The second, visionary step, requires the development of completely new ceramic structural materials and systems that can withstand surface temperatures of up to 1 400 °C required to burn the fuel with considerably higher efficiency with concurrent reduction in polluting gases. Bridging these two steps is the current coating technology that reaches its temperature limit at approximately 1 200 °C [110].

Thick thermal barrier coatings (TTBCs) satisfy requirements of thermal efficiency

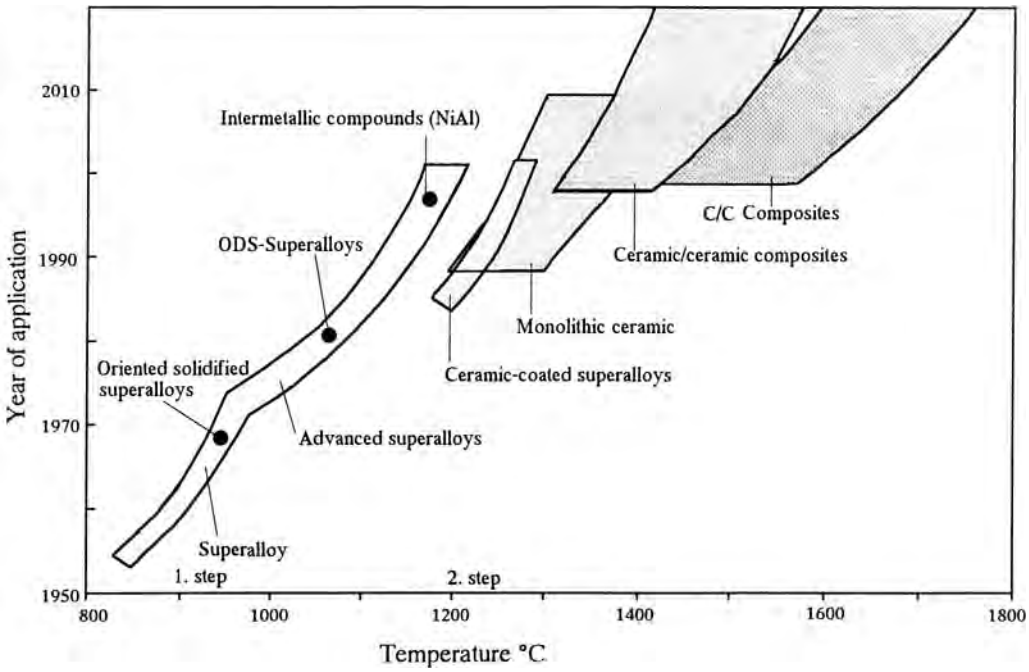

Figure 6-17. NASA scenario of development trends in in-service temperatures of aerospace gas turbines [110].

but pose problems with residual stresses that are maximized in such thick coatings (Fig. 6-18). Therefore, optimization of the ceramic material has been performed in two areas: *chemical modifications* and *microstructural modifications* [111].

As a result of *chemical modification*, the lifetime of a TBC has been maximized by varying the yttria content in zirconia. An yttria concentration of 6–8 wt. % coincides with the maximum amount of a nonequilibrium 'non-transformable' tetragonal zirconia polymorph (t′-zirconia).

State-of-the-art technology consists of applying zirconia coatings, partially stabilized with 7–8 wt. % yttria, over a metallic bond coat of Ni- or CoCrAlY alloy. The bond coat must be applied by VPS technology to prevent formation of alumina scale that is thought to reduce adhesion strength to the superalloy substrate. The PSZ top layer is generally being sprayed in the APS mode since VPS experiments have shown that in this case the PSZ layer develops Young's moduli three times larger than those observed in APS coatings [112]. Because of this larger modules thermal stresses are expected to be generated in VPS–PSZ coatings. Figure 6-19 shows the phase relationships of the binary system ZrO_2–Y_2O_3 with several compositions whose grain sizes of the t-phase, bending strengths and fracture toughnesses are displayed. In general, fracture toughness increases with decreasing amount of yttria, whereas the thermal stability increases with increasing yttria content. This requires trade-offs depending on the application of the material. For 8 wt. % (2.65 mol %) yttria the phase

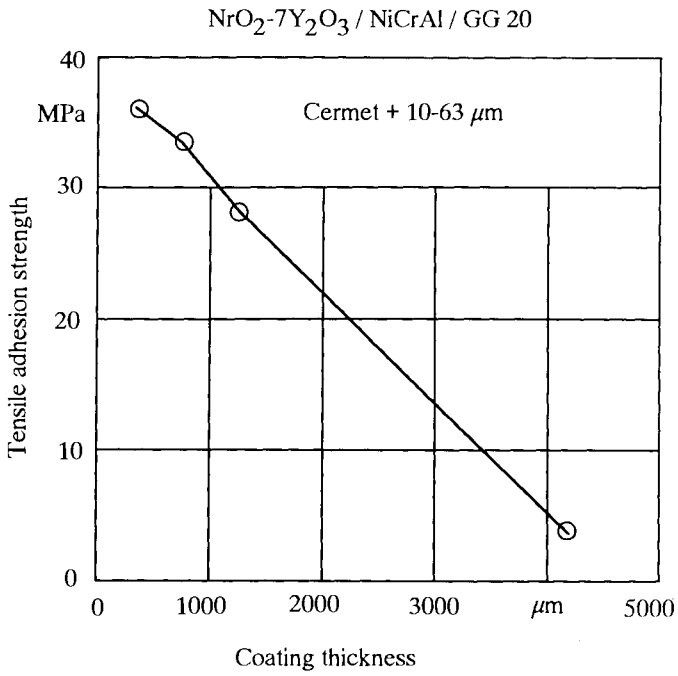

Figure 6-18. Dependence of the adhesion strength of an Y–PSZ–TBC coating on the coating thickness [132].

assembly at ambient temperature should consist of a mixture of cubic and monoclinic zirconia (Fig. 6-19). However, extensive X-ray diffraction work on as-sprayed coatings have shown a tetragonal phase and only a small amount of monoclinic phase [113–116]. This tetragonal (t′) phase does not transform to the monoclinic (m) phase because of the rapid splat cooling during plasma spraying. It is a tetragonal solid solution with high yttria content that on annealing at high temperatures (1 300 °C) transforms slowly by a diffusion-controlled mechanism to equilibrium tetragonal (t) zirconia with low yttria content, and cubic (c) zirconia [117].

A second aspect of chemical modification concerns the replacement of the stabilizing yttria by other elements. Work in this area has been rather scarce. Using ceria instead of yttria, the microhardness and crack resistance could be markedly improved for a PSZ stabilized with 15 mol% CeO_2 [118].

The *microstructural modifications* relate to porosity control. Porosity and microcrack distribution impart to the material a tolerance to thermal and residual stresses. Thus the lifetime of a TBC is sensitive to density variations that can be controlled by proper adjustment of the plasma spray parameters by statistical experimental design methodology.

Not surprisingly, most modern developments in the field of TBCs are carried out by manufacturers of aerospace gas turbine engines, i.e. Rolls–Royce [119, 120], General Electric [121, 122], NASA [123–126] and Pratt & Whitney [127] but also by plasma spray equipment manufacturers [128, 129] and superalloy suppliers [130].

The future performance profile of TBCs will include improved thermal barrier function, oxidation resistance as well as corrosion- and erosion resistance. With im-

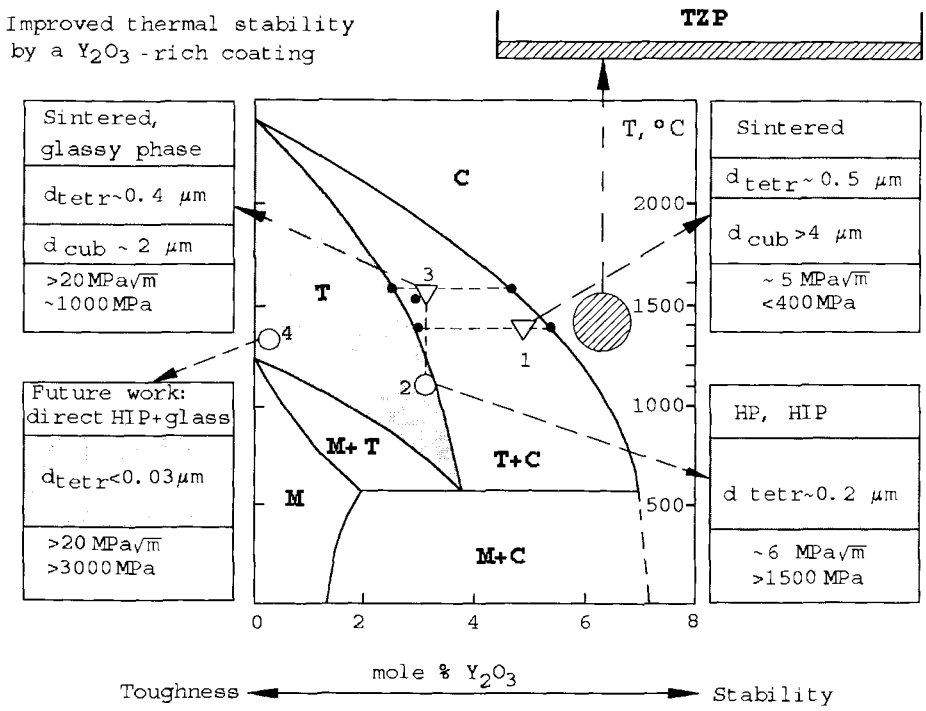

Figure 6-19. Phase relationship of the binary system ZrO_2–Y_2O_3. Different compositions for different applications are indicated (TZP: tetragonal zirconia polycrystal).

proved TBCs, economic and environmental requirements will be addressed such as higher combustion temperatures resulting in better fuel efficiency, lower cooling air requirements and hence higher compressor effectivity, and lower thermal stresses on materials that result in longer service life and maintenance cycles. There are, however, problems with TBCs that manifest themselves in increased spalling and chipping at higher operational temperatures and times. This is caused by higher residual stresses in the coatings, bond coat oxidation as well as volume changes induced by phase transformations. Here improvements are urgently needed to attain performance levels anticipated by NASA [110] for airborne gas turbines (10 000 h at turbine blade surface temperatures up to 1 400 °C), stationary gas turbines (25 000 h at up to 1 000 °C) and large stationary diesel engines (5 000 h at cycling loads).

6.2.1.1 Stress Control and Modeling

Since coated turbine section parts are subject to steep temperature gradients, high thermal shock resistance of the metallic bond coat/ceramic top coat is generally required. However, residual stresses in the as-sprayed PSZ coating arising from the difference in the CTE between the Inconel 617 substrate (CTE = 16 p.p.m. at 850 °C) and the 7% yttria–PSZ coating (CTE = 10 p.p.m. at 850 °C) decrease the thermal

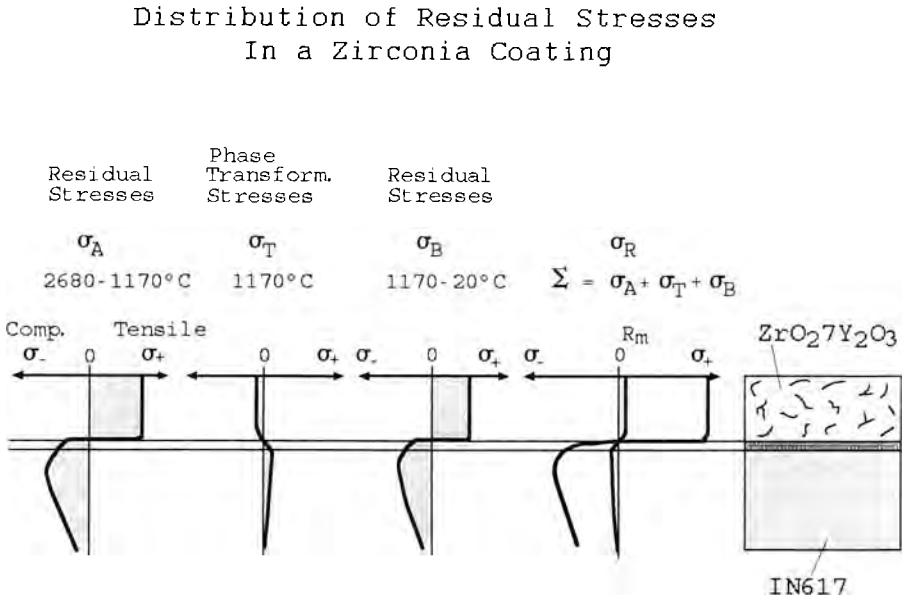

Figure 6-20. Modeling of the distribution of residual stresses in an Y–PSZ coating [131].

shock resistance, and thus the life expectancy of the TBC. Figure 6-20 shows how, in PSZ, strong shrinkage by cooling from the melting temperature at 2 680 °C to the temperature of the martensitic tetragonal–monoclinic phase transition at 1 170 °C introduces large tensile stresses in the coating [131]. The phase transition in PSZ with approximately 8% of monoclinic phase increases the volume only slightly, and thus adds some compressive component that, however, is too small to offset the strong tensile stresses introduced. Further temperature decrease to room temperature again introduces shrinkage, i.e. tensile stresses in the ceramics. Since the added-up tensile stresses exceed the yield strength of the material many times over, stress relief occurs through microcracking and/or delamination.

The NiCrAlY bond coat provides a good mechanical bond between the substrate and the ceramic coating, and also oxidation and hot corrosion (sulfidation) resistance for the substrate. Due to the routinely applied grit-blasting procedure before plasma spraying, the interface between the metal substrate and the coating is rough, and can be modeled as a quasi-sinusoidal surface. Finite element analyses [124] have shown that compressive axial and hoop stresses are located in the valleys of the quasi-sinusoidal surfaces but tensile radial stresses at the peaks of the asperities (Fig. 6-21(i)). Thus, a microcrack originating at the point of maximum tensile loading (Fig. 6-21(ii)) will be arrested once it enters a region of compression.

It has been amply confirmed that the key failure mechanism of TBCs is bond coat oxidation [111]. If the NiCoCrAlY bond coat is oxidized by penetration through the porous PSZ layer of hot corrosive gases, the signs of the axial and radial stresses are reversed (Fig. 6-22(iii)). As a result, crack extension can occur from the region of the peaks, now under compression, into the region of the valley, now under ten-

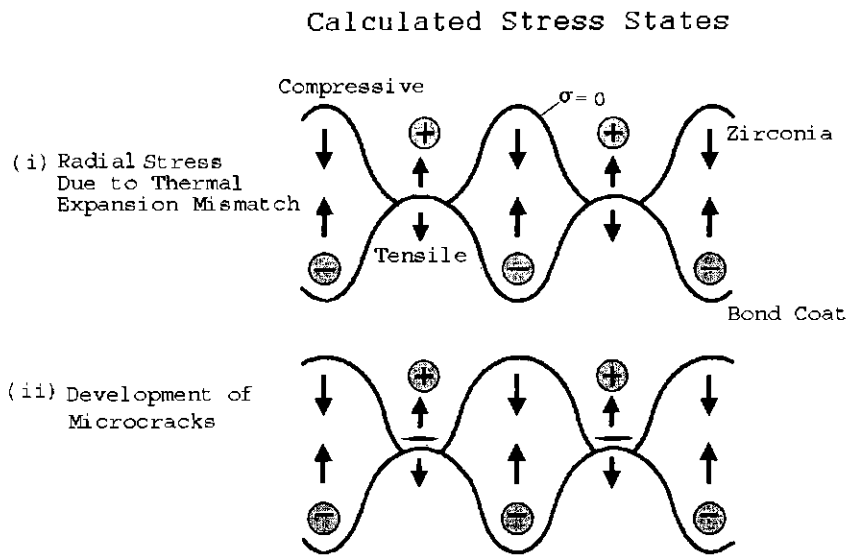

Figure 6-21. Calculated stress states in a PSZ-bond coat system with sinusoidally modeled interface [124].

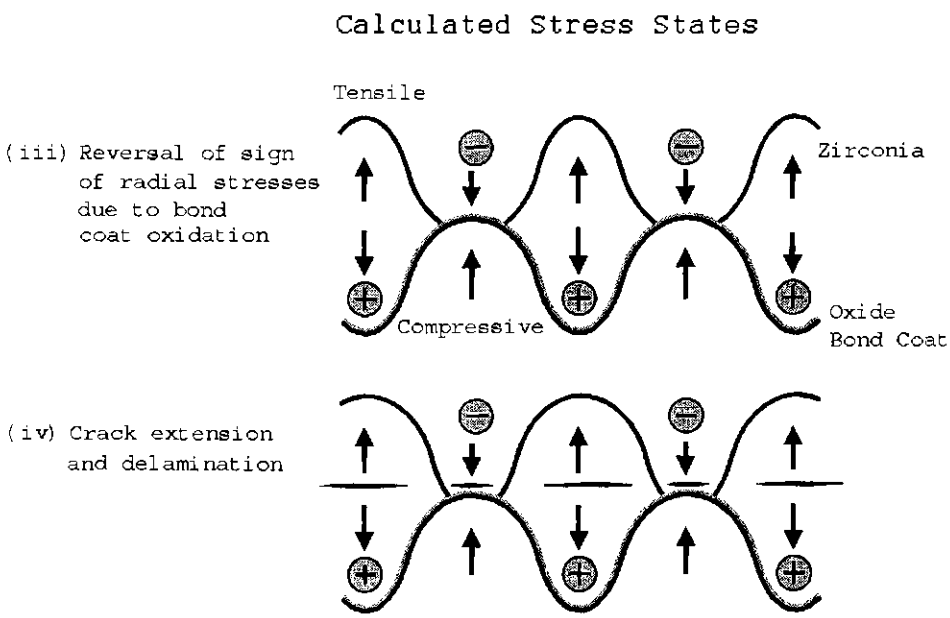

Figure 6-22. As Fig. 6-21 but with stress sign reversal due to bond coat oxidation [124].

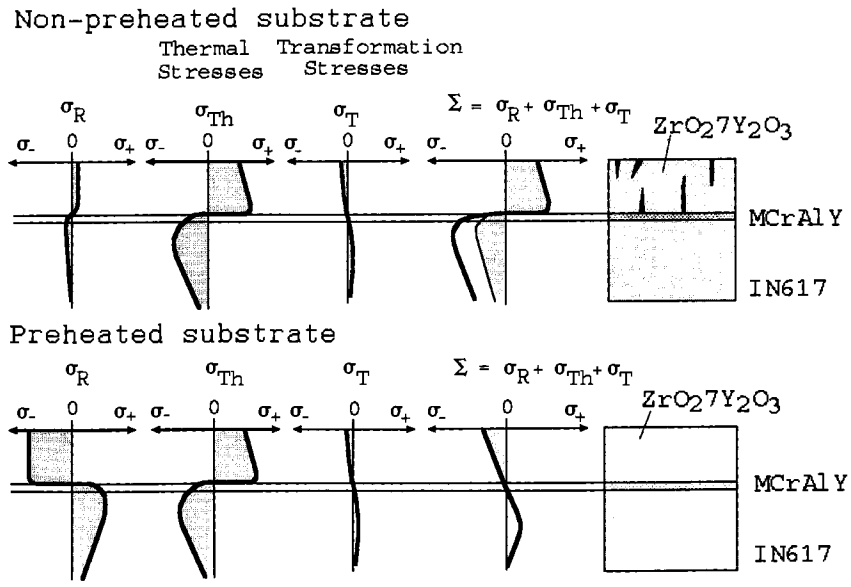

Figure 6-23. Distribution of residual stresses in Y–PSZ coatings on nonpreheated and preheated substrates [131].

sion. Hence, complete delamination or exfoliation will eventually take place (Fig. 6-22(iv)) [124].

Tackling the problem of cracking involves two aspects: Controlling the residual tensile stresses in the coating, and preventing bond coat oxidation. The first task involves the, at least theoretical, possibility of reversing the stresses in the ceramic layer on an Inconel 617 substrate from tensile to compressive by substrate preheating. Figure 6-23 shows the stress distribution during thermal shock testing of nonpreheated (top) and preheated (bottom) substrates [131]. The preheating of the IN 617 substrate induces large compressive stresses in the coating that should offset the tensile stresses occuring during cooling. As a result, a slight compressive stress component remains at room temperature thus producing a crack-free coating. However, coatings cannot be treated as a continuum bulk ceramics but are built up layer by layer in several traverses of the plasma jet. Thus every new layer acts as a heat treatment for the previously deposited one, and heat flow from the substrate decreases. It should be emphasized that this dynamic scheme of *in situ* annealing leads to a degrading of the coating, and thus largely foils any attempt to model its complete thermal history by finite element analysis. Work in this area [124] was based on the assumption of homogeneous, isotropic and linearly elastic behavior of the PSZ layer, the bond coat, and the substrate. The modulus of elasticity was assumed to be constant and time-invariant, whereas in reality it is a strong function of the porosity of the coating (Fig. 6-24, [132]). The porosity of the coatings will also affect the value of the thermal conductivity: a small change from 1.00 to 0.75 $W\,m^{-1}\,°C^{-1}$ can shift the residual stress from overall compressive to overall tensile [133].

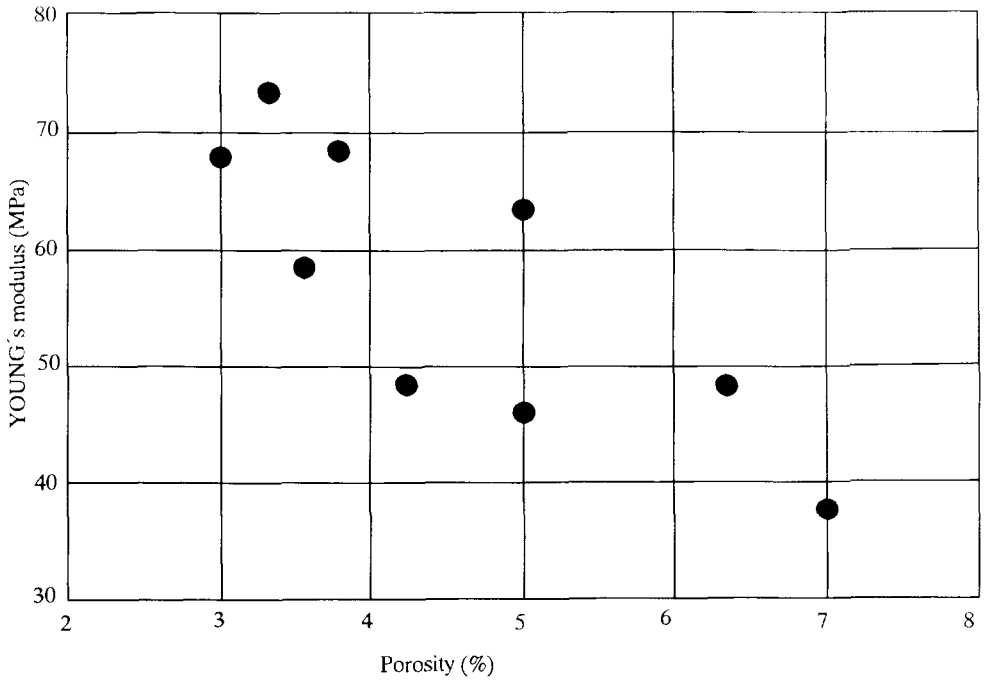

Figure 6-24. Modulus of elasticity as a function of coating porosity in Y–PSZ coatings [132].

A rough estimation of the preheating temperature required to alleviate residual tensile coating stresses can be obtained from Eq. (5-53) that determines the critical temperature difference ΔT_c between the lowest temperature of plastic flow and the preheating temperature:

$$\Delta T_c = \sigma(1 - \nu)/E\alpha \tag{6-3}$$

with $\sigma = 600\,\text{MPa}$, $\nu = 0.26$, $E = 200\,\text{GPa}$, and $\alpha = 10^{-5}\,\text{mm}^{-1}\,^{\circ}\text{C}^{-1}$. With these values, $\Delta T_c = 533\,\text{K}$, i.e. if the critical temperature difference between the lowest temperature of plastic flow (Nabarro–Herring creep) and the preheating temperature is less than 260 °C, than there is no microcracking. The Nabarro–Herring creep limit is approximately 0.6 $T_m = 0.6 \times 3133\,\text{K} = 1880\,\text{K}$. Thus the minimum preheating temperature becomes $T_p = 1880 - 533 = 1347\,\text{K}$! For a finite quench rate, the Biot modulus is $\text{Bi} = dh/k$, where d = thickness of the ceramic layer, $h = c_p \times a \times \rho/d = 3.3 \times 10^4\,\text{J s}^{-1}\,\text{m}^{-2}\text{K}^{-1}$, and $k = 1.0\,\text{J s}^{-1}\,\text{m}^{-1}\,\text{K}^{-1}$. Thus $\text{Bi} = 1.16$, $\Delta T_c = 533[\text{K}] \times 1.16 = 618\,\text{K}$; $T_p = 1262\,\text{K}$! Therefore, the minimum preheating temperature required to alleviate microcracking is close to the range of the melting temperature of the Ni-based superalloy. This is to be expected since stress relief in ceramic coatings generally requires very high temperatures owing to the non dislocation-type mechanism of lattice rearrangement.

6.2.1.2 Sealing of As-sprayed Surfaces

To prevent bond coat oxidation, sealing the surface of the porous PSZ coating can be performed in several ways.

- Spraying of the bond coat under vacuum or low-pressure inert gas conditions prevents *a priori* oxidation, and thus increases drastically the number of cycles-to-failure as compared with air plasma spraying.
- Through infiltration of the PSZ coating with hot corrosion-resistant material such as nickel aluminide or CVD-SiC, effective sealing can be achieved.
- Reduction of surface porosity by plasma-spraying a final top layer of very fine zirconia.
- Treatment of plasma-sprayed PSZ with a 0.1 mm slurry layer that is subsequently densified by a heat treatment.
- Control of porosity with adjusted powder morphology.
- Addition of Si to the MCrAlY bond coat to improve its oxidation/corrosion resistance.
- Plasma-spraying of low yttria PSZ whose expansion during the martensitic t–m transition offsets the thermal contraction.
- Laser surface remelting ('laser glazing').
- Reactive laser treatment with alumina and silica to produce dense, low melting eutectic compositions.
- Hot isostatic pressing.

6.2.1.3 Laser Surface Remelting of Y-PSZ Coatings

Laser glazing provides a smooth, dense top layer but tends to introduce cracks owing to nonuniform cooling after the point-like introduction of heat through the focused laser beam. Figure 6-25a–c shows scanning electron micrographs of plasma-sprayed Y-PSZ (Plasmalloy grade AI-1075)/NiCoCrAlY (Plasmalloy grade AI-1065-2; right border) 'tandem' plasma-sprayed with an argon/helium plasma jet at an arc current of 800 A (NiCoCrAlY) and 900 A (Y-PSZ), respectively. Figure 6-25a shows the as-sprayed TBC with a typically rough and detailed surface, large pores close to the surface as well as a network of radial (transverse) and layer-parallel (longitudinal) microcracks. Laser treatment was performed with a Mitsubishi CO_2–CW laser with a power of 1 kW, a beam diameter of 3 mm, and a wavelength of 10.6 μm [134]. Figure 6-25b shows the result of laser glazing using a laser beam scanning speed of 23 cm s^{-1} that translates to a laser irradiance (energy density) of 1.45 J mm^{-2}. The surface is smooth and essentially free of pores down to a depth of 30–40 μm. Increasing the laser energy density to 3.33 J mm^{-2} (Fig. 6-25c) results in pronounced cracking. This, however, is not necessarily deleterious to the performance of the TBC since laser-induced *radial cracks* may increase the mechanical stability and the fracture toughness, respectively by a crack arresting mechanism thus leading to a strain-tolerant toughened ceramics. They also constitute sinks for thermal stresses introduced by the differences in the coefficients of thermal expansion. On the other hand, transverse cracks are oriented parallel to the heat flux,

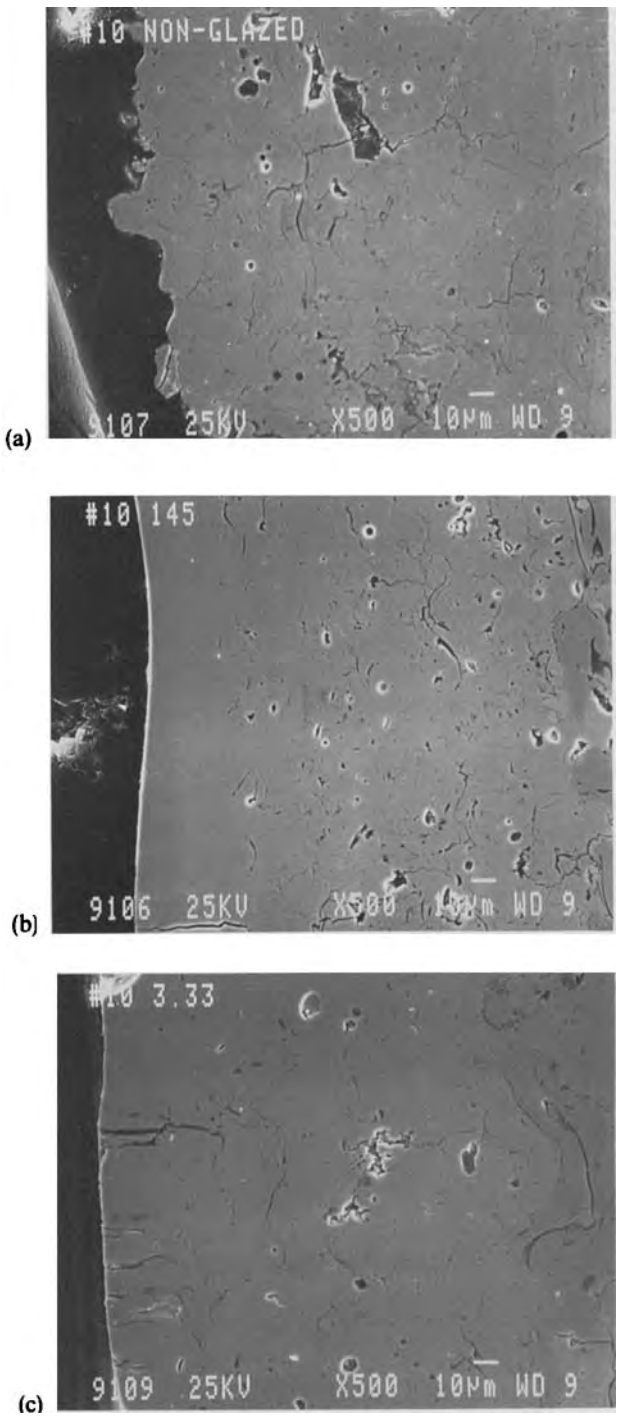

Figure 6-25. SEM micrographs of as-sprayed (a) and laser-remelted (b: laser irradiance: 1.45 J mm^{-2}; c: laser irradiance: 3.33 J mm^{-2}) Y–PSZ coatings [134].

and this results in a maximum value of the thermal diffusivity. Effective thermal diffusivity values a_{eff} are

$$a_{\text{eff}} = a_0(1 + 8Nb^3/3)^{-1} \text{ for cracks perpendicular to the heat flux} \quad (6\text{-}4a)$$

$$a_{\text{eff}} = a_0(1 + 8Nb^3/9)^{-1} \text{ for randomly oriented cracks} \quad (6\text{-}4b)$$

$$a_{\text{eff}} = a_0 \text{ for cracks parallel to the heat flux,} \quad (6\text{-}4c)$$

where a_0 = bulk thermal diffusivity, N = number of cracks, and b = f(crack radius). With increasing layer thickness, both radial and longitudinal cracks will be formed. Longitudinal cracks appear to delineate splat boundaries and are thus undesirable since they tend to increase the risk of delamination and exfoliation of the coatings. On the other hand, they also limit the transverse crack propagation. It was found that despite such cracking the lifetime of laser-densified coatings in corrosive thermally cycled burner rig tests can increase by a factor of three to ten, depending on the coating thickness [135]. A problem, however, exists since the surface cracks are known to act as nuclei for subsequent cavitational erosion damage [136].

It should be noted that the specific laser energy density required to melt a ceramic material is much lower than that needed to melt a metal. This can be related to the lower reflectivity and the lower thermal conductivity of ceramics compared to a typical metal. The Cline–Anthony model for a moving Gaussian laser beam to calculate the depth of the melt pool is not applicable [137] since the high scanning rate (15 to 30 cm s^{-1}) of the laser beam renders the temperature distribution asymmetric in the direction of the beam traverse. Figure 6-26 (top) shows the temperature profile that can be approximated by a Gaussian distribution, $T = T_0 \exp(-x^2/2R^2)$, where R = radius of the laser beam. Due to the low thermal conductivity of the material, the molten ceramic pool does not cool instantaneously, and a pronounced asymmetry develops. The figure shows also the onset of surface rippling associated with surface-tension gradients [138]. Also, in the ceramic layer under the center of the laser beam depressions develop (Fig. 6-27b). Their origin is related to such surface-tension gradients induced by a temperature difference between the center of the beam and the regions further away from it. In the center, the temperature of the melt is at its maximum and thus the surface tension at a minimum. As the temperature decreases away from the center, the surface tension increases. This pulls away the melt from the center thereby depressing the surface under the beam and raise the melt level at the periphery of the melt pool (surface 'rippling', Fig. 6-26, top). As the height difference increases, a pressure head develops that will eventually induce a gravity-driven counterflow (Fig. 6-26, bottom). At steady state, the liquid flow away from the beam center, driven by the surface-tension gradient, will be exactly balanced by the gravity-driven counterflow towards the beam center[2].

Increase of the laser irradiance from 0.34 (Fig. 6-27a) to 1.45 (Fig. 6-27b) to 3.33 J mm^{-2} (Fig. 6-27c) leads to more pronounced cracking. Also, as shown in Fig.

[2] This mechanism is identical to the mechanism responsible for the formation of wine 'tears' where a surface-tension gradient, produced by evaporation of alcohol, exerts a shear stress on the surface of the liquid that drags it up the sides of the wine glass.

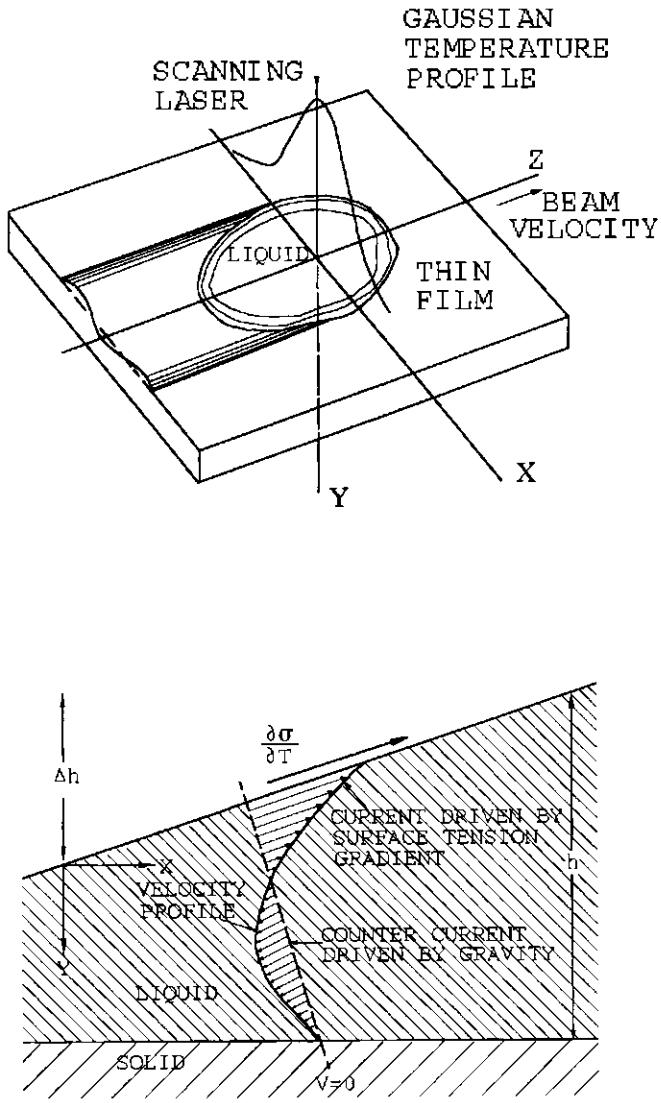

Figure 6-26. Temperature profile of a scanning laser beam (top) and explanation of the onset of surface 'rippling' due to a strong gradient in surface tension (bottom) [138].

6-27b the depths of the laser-induced depressions increase with decreasing scanning speed (top to bottom). It is therefore mandatory to optimize the specific laser energy for sealing of coatings. Experiments have shown [139] that at high laser irradiance two solidification fronts exist in the laser-melted coating, one originating at the melt/substrate interface and one at the melt/air interface. The former is related to conductive heat losses, the latter to radiative heat losses. Which front will overtake the other depends on the laser power. Also, the appearance of the remelted layers are

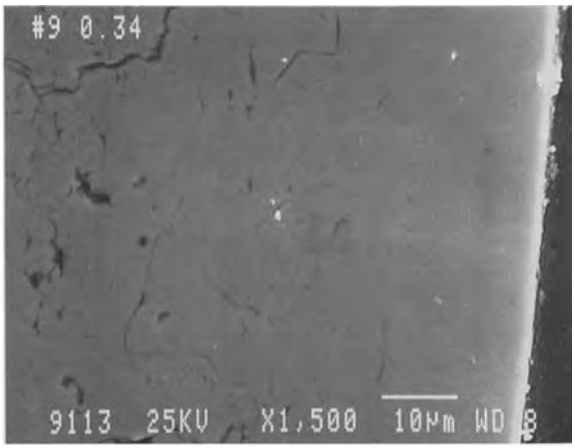

(a)

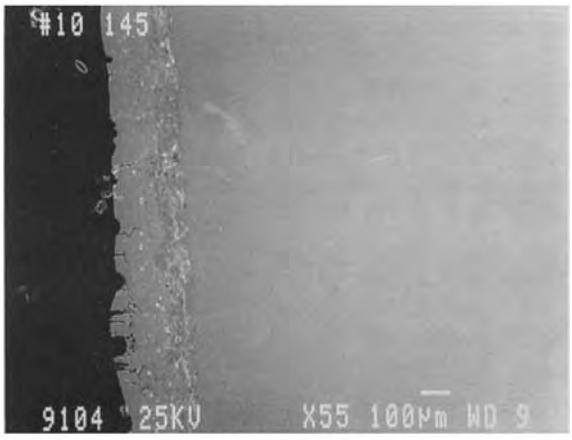

(b)

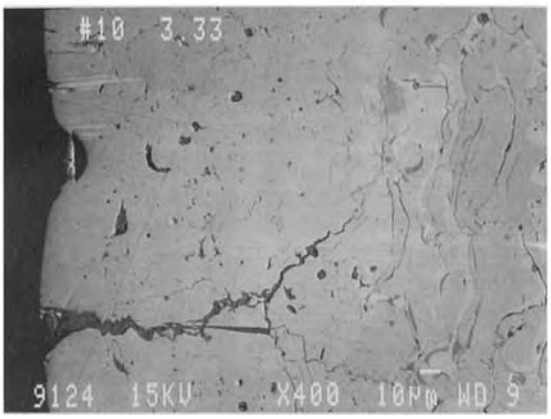

(c)

Figure 6-27. Increase of radial cracking with increasing laser irradiance (a: 0.34 J mm^2, b: 1.45 J mm^{-2}, c: 3.33 J mm^{-2}) [134].

different: equiaxed grains in case of radiative heat loss, columnar grains in case of conductive heat loss.

Two other treatments have been explored with the objective to reduce coating cracking: pulsed laser sealing and reactive laser treatment. Experiments with *pulsed lasers* [140] revealed that although microcracking could be only slightly reduced the resulting coatings showed less depressions, smoother surfaces, and improved thermal shock resistance, particularly when laser-glazing was preceeded by sample preheating. The extremely rapid solidification stabilizes the nontransformable tetragonal zirconia (t′) phase [141]. The amount of the cubic equilibrium phase decreases. Nontransformable tetragonal zirconia contains a high amount of yttria in solid solution, and during laser remelting there is not enough time available to redistribute yttria by diffusion to form the equilibrium t-phase with low yttria content. On annealing such a laser remelted coating, the t′-phase transform indeed to $(t + c)$ phase. The maximum rate of transformation has been found to occur at 1400 °C as represented in a time–temperature–transformation- (TTT) diagram [116].

A promising *reactive laser sealing* approach was put forward by Petitbon *et al.* [66] by feeding alumina powder directly into a laser beam through a modified nozzle of a 3 kW CO_2 laser. A eutectic alumina–zirconia top layer was formed that produced a smooth, dense and very hard (20 GPa) surface layer with reduced microcracks that shows greatly improved wear- and erosion resistance and may thus be applied to improve coatings for turbine airfoils and diesel engine valves.

In conclusion, laser surface-engineering of plasma-sprayed thermal barrier coating systems is necessary to improve their performance in terms of high-temperature corrosion, wear- and thermoshock resistance for demanding applications including those in the aerospace and automotive industries. Laser surface remelting and reactive laser treatment are modern techniques that need more work and, in particular, the synergistic interaction of various scientific and engineering disciplines. Since laser equipment is predominantly operated by physicists, materials scientists must become more conversant in laser physics, and *vice versa*, physicists must better understand the specifics of ceramic engineering. Only then can the tremendous challenges be overcome that are being posed today by ceramic thermal barrier coatings.

6.2.2 Other Thermal Barrier Coatings

The search for other ceramic materials to be used as thermal barrier coatings was triggered by the still large difference in the coefficients of thermal expansion between base metal and ceramic coating that tend to introduce large thermal and residual stresses. Coatings consisting of dicalcium silicate (C_2S) over a NiCrAlY bond coat on stainless steel (SUS-304) revealed a higher coefficient of thermal expansion compared to PSZ (13 p.p.m. *versus* 9 p.p.m.), good thermal shock resistance, excellent hot corrosion resistance against V_2O_5 and Na_2SO_4 as well as a small thermal conductivity comparable or even less than PSZ [142].

A second line of investigation deals with the ternary system $CaO–SiO_2–ZrO_2$, i.e. $C_2S–CZ$. The high temperature oxidation behavior up to 1100 °C of these coatings is characterized by a lack of exfoliation and severe cracking that has been observed in

PSZ TBCs under comparable conditions. Instead, a reaction layer develops, presumably by involvement of Al and/or Cr from the bond coat underneath. In hot corrosion tests involving molten salts, the new coating behaved quite poorly, and showed high reactivity at temperatures around 1000 °C [143].

6.3 Bioceramic Coatings

Research and development on bioceramic materials have reached a level of involvement and sophistication comparable only to electronic ceramics. The reason is clear: large proportions of an aging population rely increasingly on bone replacement ranging from alveolar ridge augmentation to hip endoprostheses. Ceramics based on calcium phosphates such as $C_{10}P_3H$ (hydroxyapatite, HAp) or C_3P[3] are prime candidates for both replacement of bone subjected to low loading conditions and osseoconductive coatings of the femoral shafts of hip prostheses and dental root replacement parts [144].

Bioactive ceramics, for example calcium phosphates and bioactive glasses, not only interact with the body by stimulating osseointegration but will sometimes also be resorbed and transformed to calcified osseous tissue. The dominating biorelevant mechanism is bonding osteogenesis characterized by a chemical bond between implant and bone. Bioinert materials such as alumina, zirconia, carbon and also some metals like titanium or tantalum react to the host bone by contact osteogenesis characterized by a direct contact between implant and bone. Biotolerant materials such as bone cement (polymethylmethacrylate, PMMA) and also stainless steel and Co–Cr alloys will be accepted by the body and develop an implant interface characterized by a layer of connective tissue between implant and bone thus resulting in a distance osteogenesis.

The application of bioactive calcium phosphate ceramics is generally restricted to non-load-bearing areas because of their low fracture toughness and limited modulus of elasticity. To counteract this drawback calcium phosphate coatings are being applied to load-bearing metallic parts thus creating a synergistic composite of a tough and strong metallic substrate providing strength, and a porous bioactive HAp coating providing osseointegration function. In fact, many *in vivo* investigations have shown that a coated implant is readily accepted by the body and develops within a few weeks a type of bonding osteogenesis with the surrounding bone. Uncoated implants react by a distance osteogenetic mechanisms developing a connective tissue layer at the interface [145, 146]. Films of a few μm thickness have only a limited application for stimulating bone in-growth but may be beneficial for their self repair function in contact with aggressive body fluids. Thick plasma-sprayed HAp coatings [147] are now being applied routinely to the shafts of hip endoprosthetic devices and

[3] Here the cement chemistry notation will be used: $A = Al_2O_3$, $C = CaO$, $P = P_2O_5$, $S = SiO_2$, $H = H_2O$, $T = TiO_2$ etc.

to dental root implants. Their preparation, however, requires a high degree of skill, and general principles of total quality management must be adhered to. Important factors of HAp coating performance include chemical composition, i.e. purity (HAp content >98%, heavy metal content <50 p.p.m. [148]), Ca/P molar ratio (>1.67), crystallinity of the deposit, phase purity, microstructure, i.e. density, adhesive strength to the metal substrate, and coating thickness. Optimization of these factors are required to assure that the long-term *in vivo* performance of the coatings will not be compromised.

The positive behavior of HAp-coated metallic implants has triggered intense research into the development of appropriate coating techniques. Because of the vital importance of such bioceramic thin and thick coatings, a brief review of other than plasma-spray techniques will follow [155].

6.3.1 Thin Film Techniques for HAp Coatings

6.3.1.1 Ion Beam Dynamic Mixing

This technique has been used to produce amorphous HAp layers on a titanium substrate [149]. The layers transform during short tempering (1 h) in air at 873 K to a crystalline structure. Advantages of such layers include high adhesive strength and self repair function. Photoelectron spectroscopic investigations of a pristine and a HAp-coated titanium surface both treated for 30 days with a simulated body fluid (Hank's solution) showed that even though the thin (~ 1 μm) HAp coating has been completely dissolved within one day an extremely thin well-adhering Ca–P–Ti–OH layer remained at the surface [149].

6.3.1.2 RF Sputtering

Glassy sputter targets with varying Ca/P ratios were used to deposit thin amorphous calcium phosphate layers onto titanium substrates [150]. Dependent on the C/P ratio and the water vapor partial pressure, stoichiometric HAp or defect apatites with both Ca and OH vacancies were formed. At a C/P ratio below 0.4 no HAp forms, not even in an atmosphere containing large amount of water vapor.

6.3.1.3 Liquid Immersion Techniques

Thin dense and homogeneous HAp layers grow on a metallic (titanium) or ceramic (alumina) substrate in contact with a C–S glass submerged in a simulated body fluid containing phosphate [151]. While the technique allows growth of HAp coatings on any substrate the process is quite slow so that rather long times are required to deposit coatings of appreciable thicknesses.

6.3.1.4 Electrophoretic Deposition

The deposition is performed in a calcium phosphate suspension [152]. Once deposited the layer is being heat treated in vacuum to enhance the adhesion to the tita-

nium substrate. During this process hydroxyl groups are partly lost from the structure and a mixture of hydroxyapatite, $Ca_{10}[(OH)_2(PO_4)_6]$, oxyhydroxyapatite, $Ca_{10}[O(PO_4)_6]$ and tetracalcium phosphate, $Ca_4[O(PO_4)_2]$ forms. This was documented by Fourier transformed infrared spectra of a HAp with Ca deficit after sintering for 2 h in vacuum as well as after an electrophoretic deposition and sintering in vacuum. In both cases the phonon spectra did not show the infrared bands characteristic of the OH group at 3571 and 633 cm^{-1} but showed instead bands in the range of 550–610 cm^{-1} attributed to oxyhydroxyapatite [153].

6.3.2 Thick HAp Coatings

Thick coatings can be applied to titanium alloy substrates by essentially three methods: powder sintering, powder adhesion by glueing, and plasma spraying. In this context only plasma-spraying will be considered.

6.3.2.1 Plasma Sprayed HAp Coatings

This process constitutes the state-of-the-art procedure to improve the biological integration of implants into the body. Techniques applied include atmospheric plasma spraying (APS), flame spraying, high velocity oxyfuel flame (HVOF) spraying [154], and occasionally, vacuum plasma spraying (VPS) [155]. Both hydroxyapatite (HAp) and fluorapatite (FAp) can potentially be deposited by plasma spray techniques. FAp in particular does not decompose in the plasma jet compared to HAp that tends to form C_3P or C_4P by thermal decomposition (see below). Also, plasma spray-deposited FAp coatings show a high degree of crystallinity [156]. Histologic and histomorphometric investigations of coatings implanted in animals show, however, that in contrast to HAp the FAp coatings are intensely attacked by soft tissue [157]. In addition, the in-growth of bone cells into the porous FAp coatings is much suppressed [158]. Obviously, fluoride ions released from the coatings cause a cytotoxic response and thus hamper implant integration. This excludes FAp from the list of biocompatible ceramics. It should be mentioned that in the vicinity of uncoated titanium implants significant titanium ion concentrations were measured because of the extremely aggressive body environment. Even though at this time this accumulation of titanium ions is being considered nontoxic, an implant coated with HAp seems to provide a more benign environment in which only Ca and P ions concentrate [148].

Spraying of HAp is performed worldwide under widely varying conditions [154, 155, 159–162] resulting in coatings differing in their phase purity, adhesion strength and crystallinity. The control of these coating properties is crucial: HAp shows during *in vitro* as well as *in vivo* tests a significantly higher stability than C_3P and C_4P. Since also the resistance to resorption increases with increasing crystallinity, and proper adhesion of the coating to the metal implant prevents the invasion of acellular connective tissue leading potentially to a loosening of the bond to the bone, optimization of the three responses is vital.

Vacuum plasma spraying of highly crystalline, phase-pure HAp coatings with maximum adhesion to Ti6Al4V substrates led to new insight into the deposition

mechanism [155]. Research is also in progress to design biocompatible bond coats to increase the adhesion of the HAp coating to the substrate, prevent release of Ti ions, prevent direct contact of the HAp with the Ti alloy that appears to promote decomposition of HAp, and reduce the fast removal of heat and thus prevents the formation of a rapidly quenched amorphous contact layer immediately at the titanium interface [155].

Parametric study of HAp coating properties

The high temperature of the plasma jet promotes, even during the very short residence time of the HAp powder particles in its hot zone, a noticeable decomposition towards C_3P and C_4P or even CaO. The calcium phosphate phases occuring in the sprayed samples are compatible with the phase diagram shown in Figure 6-28 that indicates decomposition of HAp above 1360 °C [163]. The stability of HAp is also a function of the water vapor partial pressure, p_{H_2O} of the surrounding atmosphere (Fig. 6-28). The temperature representing the equilibrium HAp + CaO → HAp + C_4P + H_2O increases with increasing water vapor partial pressure, i.e. at a given temperature and a higher p_{H_2O} is the phase assembly HAp + CaO more stable than HAp + C_4P.

The powder feed rate, m, influences the heat transfer from the plasma to the powder particles, i.e. at the same plasma energy, η, the thermal decomposition of the HAp decreases with increasing powder feed rate. By the same token HAp decomposition is minimized at low substrate temperature, T_s, increasing chamber pressure, P, and increasing stand-off distance, X. On the other hand, optimizing the coating adhesion requires a reduction of residual stresses, σ, in the coating. This can be achieved at low plasma energies, η, high substrate temperature, T_s, and low stand-off distance, X.

The high substrate temperature promotes diffusion of Ti into the coating and leads to an increase in thickness of the reaction layer found to consist of CT (perovskite) [147] and/or CT_2 [164]. This thicker reaction layer in turn reduces the thermal decomposition of subsequently deposited HAp layers [152, 165]. Under these conditions the sprayed HAp layer attains a brown color thus supporting the ideas of an increased Ti diffusion. The brown color disappears after heat treatment at 800 °C in air for 2 h possibly by oxidation of Ti^{3+} originally formed in the reducing argon/hydrogen plasma [155].

Increasing the chamber pressure, P, produces a shorter plasma jet so that at a constant stand-off distance, X, lower surface temperatures occur. This in turn suppresses the thermal decomposition of HAp.

Parametric VPS experiments performed on HAp powder with different plasma energies, η, powder feed rates, m, stand-off distances, X, chamber pressures, P, and substrate preheating, T_s, revealed the following coating optimization strategies.

- To suppress thermal decomposition of HAp the enthalpy supplied to the powder and the coating, respectively must be reduced. This can be done effectively by minimizing the plasma power, η, and the substrate temperature, T_s, but maximizing the powder feed rate, m, the stand-off distance, X, and the chamber pressure, P.

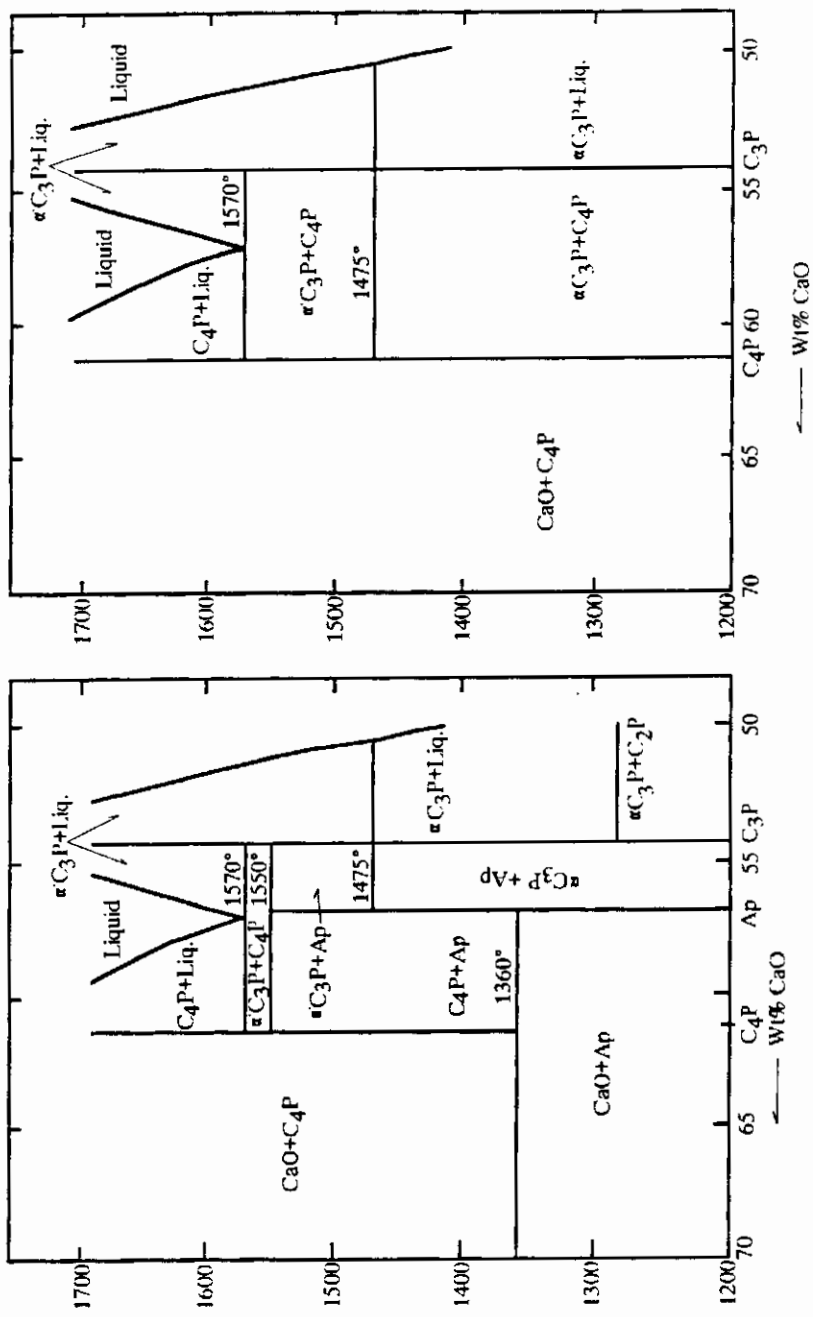

Figure 6-28. Central portion of the phase diagram $CaO–P_2O_5$ in air (right) and with a water vapor partial pressure of 0.67 atm (left) [163].

- To reduce the coating porosity but retain its biological functionality the enthalpy supplied to the powder must be increased by both increasing the plasma power, η, and the substrate temperature, T_s, but minimizing the stand-off distance, X.
- Finally, to optimize the coating adhesion both the plasma power, η, and the stand-off distance, X, should be minimized but the substrate should be preheated to alleviate the gradient of the coefficients of thermal expansion between coating and substrate, and hence the residual stresses introduced during cooling.

As it turns out, the simultaneous fulfillment of these three conditions is clearly impossible and the production of HAp coatings on Ti6Al4V implants optimized in terms of phase purity, porosity and adhesion requires a parameter and property trade-off.

Optimization studies

Based on the parametric studies reported above, attempts were made to optimize the coating properties with regard to minimizing the thermal decomposition and maximizing the coating adhesion [155]. The strategy selected was to reduce the plasma power η to 29 kW thus avoiding decomposition of HAp, and to reduce the stand-off distance X to 150 mm and 190 mm, respectively to retain a sufficient particle plasticity. Figure 6-29a shows the dense although cracked microstructure of such a coating that should be compared to that of a sample obtained with a plasma power of 42 kW (Figs. 6-29b and c). The former, however, contains only traces of C_4P whereas the latter has substantially decomposed forming large amounts of C_3P and C_4P (Fig. 6-30).

Adhesion strengths tests (ASTM C 633-79) using Araldite AV 118 as an adhesive of the optimized samples give values of 60–70 MPa, much higher than those of the samples sprayed with high plasma power that show values generally <20 MPa. The adhesion strength results for HAp coatings produced at comparable deposition conditions and reported in the literature span a wide range from 10 to 70 MPa [159–162, 166]. The deviations have been explained by the application of varying test procedures [145] as well as utilization of different adhesives [161]. There exist two contradictory opinions. First, penetration of the adhesive into the open pores of the HAp coatings will increase the adhesion so that the lower range of 10 to 20 MPa should be assumed a realistic estimate of the true adhesion strength [161]. Second, the low viscosity adhesive entering the open pores will create stresses during curing and thus weakens the microstructure of the coating, resulting in a decrease of the adhesion strength. Thus the high range of measured strength values around 70 MPa should be considered realistic [160]. If the latter is true than an adhesion strength of 70 MPa approaches the limit of bending strength (100 MPa) of HIPed high-density HAp ceramics. Push-out tests of HAp-coated implants after 3 months implantation yielded intermediate values. For example, Klein *et al.* [145, 167] reported values of around 34.5 MPa pointing to a rather strong bonding between coating and substrate, respectively and osseous hard tissue. In conclusion, a standardized test for *in vitro* and *in vivo* measurements of the coating adhesion strength is urgently needed to arrive at comparable data.

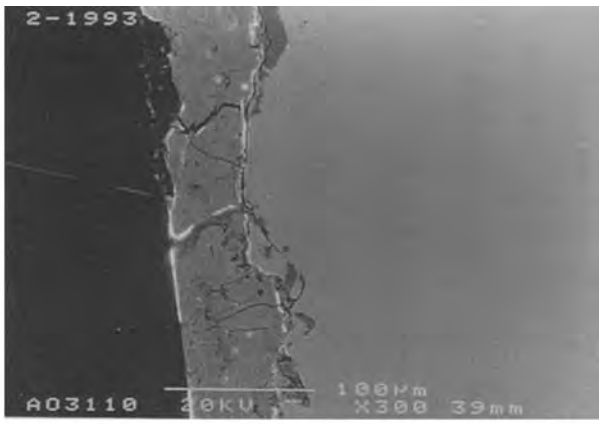

(a)

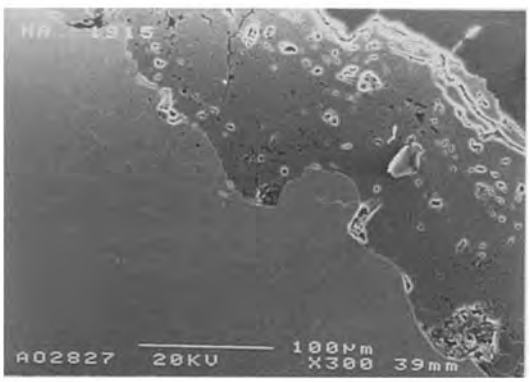

(b)

(c)

Figure 6-29. Hydroxyapatite coatings sprayed with low plasma power of 29 kW (a) and higher plasma power of 42 kW (b,c) [155].

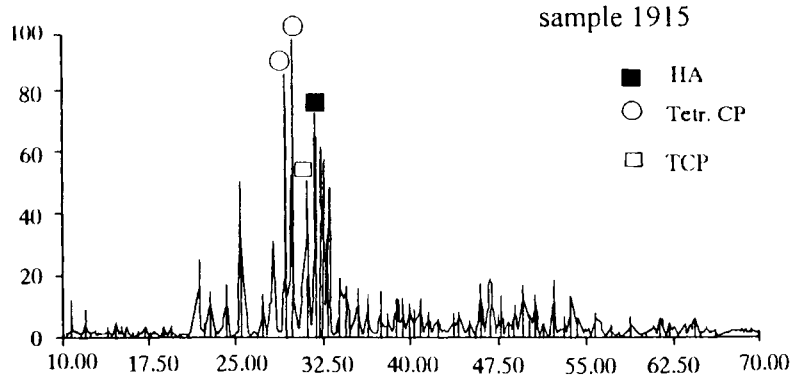

Figure 6-30. X-ray diffraction diagram of hydroxyapatite deposited by VPS at 42 kW shows pronounced decomposition into C_3P and C_4P [155].

Laser Raman spectra of selected optimized HAp coatings show a strong Raman shift of 961 cm^{-1} and weak intratetragonal bands at 430, 600 and 1050 cm^{-1} all attributed to crystalline hydroxyapatite, and a shoulder at 949 cm^{-1} thought to originate from amorphous hydroxyapatite [153].

Other coating techniques

Despite some attempts to improve the HAp-coatings by selecting HVOF [168, 154] and RF ICP techniques [169] the results were not very convincing. HVOF thermal spraying reduces powder losses in the flame because of the short residence time, and produces coatings with high crystallinity but leads to rather low adhesion (<18 MPa) and some decomposition as shown by the presence of C_3P and C_4P in the coatings. Inductively coupled-plasmas avoid contamination of the coating by W and Cu used as electrode materials in the d.c. plasmatrons but lead even at low plasma powers between 3 and 12 kW to pronounced decomposition of HAp owing to the long residence time of the particles in the plasma with free-stream velocities typically around 10–30 m s^{-1}. The long residence times of the powder compared to a d.c. plasma or HVOF system leads to intense particle heating and thus decomposition. Also, a low adhesion strength of only 5–14 MPa may be attributed to the low plasma velocities that impart only low momentum to the particles.

Future development trends

From the parametric studies of the dependence of the coating properties on the levels of the five parameters varied in the tests the following conclusions can be drawn.

1. Thermal decomposition of hydroxylapatite (HAp) starts in air above 1360 °C.
2. At identical plasma powers η an increase of the powder feed rate m causes a decrease of the thermal decomposition of HAp.
3. At identical plasma powers η and chamber pressures P an increase of the stand-off distance X causes a decrease of the thermal decomposition of HAp.

4. At identical plasma powers η, powder feed rates, m, and stand-off distances, X, a decrease of the chamber pressure, P, causes a decrease of the thermal decomposition of HAp.
5. At identical plasma powers η, powder feed rates, m, stand-off distances, X, and chamber pressures P a preheating of the substrate with the plasma jet causes increased thermal decomposition of HAp.
6. At identical stand-off distances, X, chamber pressures, P, and powder feed rates m an increase of the plasma power η causes increased thermal decomposition of HAp.

From this a catalogue of future research and development requirements can be deduced. This includes the following.

1. Minimizing thermal decomposition of plasma-sprayed HAp.
2. Minimizing coating porosity with concurrent maintenance of their biofunctional properties.
3. Maximizing crystallinity of the coatings and thus *in vivo* stability and resorption resistance.
4. Maximizing fracture toughness of coatings.
5. Maximizing coating adhesion by proper parameter optimization and/or appropriate bond coats.

6.4 Functional Plasma-sprayed Coatings

6.4.1 HT-superconducting (HTSC) Coatings

Plasma-sprayed HTSC coatings were developed with a variety of materials, among them Y–Ba–Cu–oxide [170, 171] and Bi–Sr–Ca–Cu–oxide [172]. One of the first attempts were undertaken by IBM's Yorktown Heights Laboratory to use thermal spraying to create simple integrated circuits [170]. The technique involved ionizing a jet of a powdered mixture of the starting oxides in an electric arc close to the substrate surface. Spraying through a mask or template resulted in thin strips of HTSC ceramics that were supposed to provide loss-free links between chips in computers cooled with liquid nitrogen. Major problems to overcome included stringent oxygen control to assure compositional integrity, and dimensional control to prevent overspraying and to guarantee the accuracy of the sprayed pattern.

Oxygen control indeed is one of the major weak points in plasma-spraying HTSC coatings. Precursor Y–Ba–Cu–oxide material of nominal composition $YBa_{2.06}Cu_{4.13}O_x$ ($6.6 < x < 7$) resulted in oxygen deficient coatings with a bulk composition of cubic $YBa_{2.04}Cu_{2.98}O_{5.6}$ [172] pointing to a considerable loss of Cu_2O during plasma-spraying. Heat treatment in oxygen at 875 °C for 20 h led to the formation of superconducting orthorhombic $YBa_2Cu_3O_x$ ($x = 7 \pm 0.1$) with a very fine-grained, relatively dense microstructure. a.c. susceptibility data for this sample showed an

onset of superconductivity at 90.4 K and a critical current density (shielding current) j_c at 77 K of 460 A cm^{-2}. This low value is expected since the splat structure of a plasma-sprayed coating provides for many weak links. Moreover, it is surmised that the splats are far from being uniformly conductive throughout their granular structure but that only a rather thin shell of a few micrometer thickness around each 20–50 μm splat is superconducting.

A somewhat easier way to produce HTSC coatings with the required stoichiometry and oxygen deficiency to ensure higher critical current densities may be to use liquid precursors fed into the reaction chamber of an RF inductively-coupled plasma system [173–176].

6.4.2 Coatings for Solid Oxide Fuel Cells (SOFCs)

Fuel cells convert chemical energy stored in the fuel directly to electrical energy through an electrochemical reaction and are thus considered by many one of the most advantageous energy conversion systems of the future. They combine high energy conversion efficiency (>60% for SOFCs with bottoming cycle), flexibility in fuel use, and cogeneration capability with very low chemical and acoustic pollution of the environment.

An SOFC consists of several layers with specific functions. Figure 6-31 shows the working principle. The anode (fuel electrode) consists of Ni or a Ni–Al_2O_3 or NiAl–ZrO_2 composite material. It is separated from the cathode (air electrode), made from Sr-doped lanthanum composite oxide ($LaMnO_3$, $LaCoO_3$, $LaSrMnO_3$) with perovskite structure, by the Y-stabilized zirconia electrolyte. The arrangement of these three layers ('PEN', Positive electrode–Electrolyte–Negative electrode) can be tubular, monolithic or in a flat plate configuration (Fig. 6-32). The PENs are

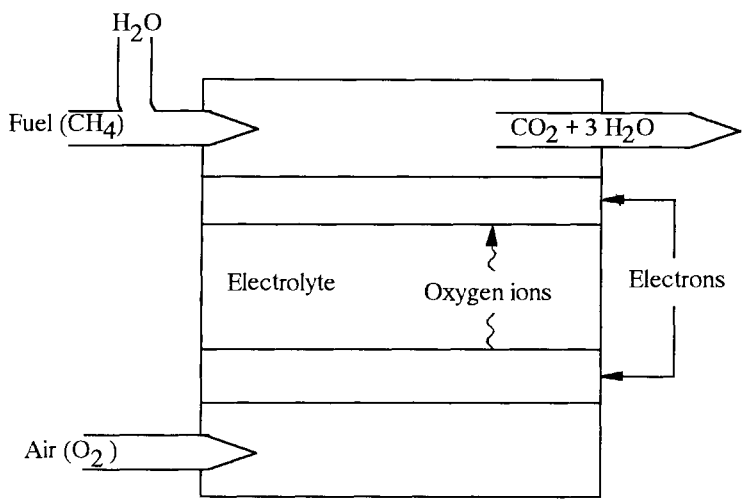

Figure 6-31. Working principle of a solid oxyde fuel cell (SOFC).

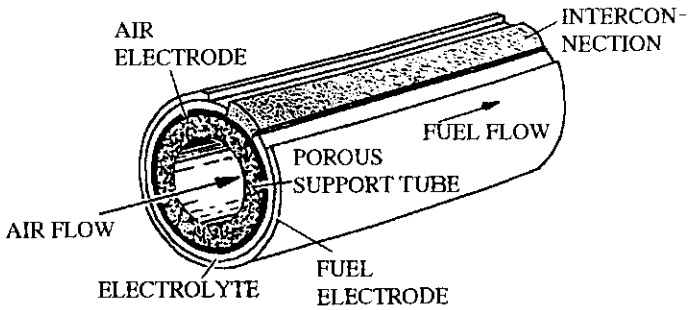

(a)

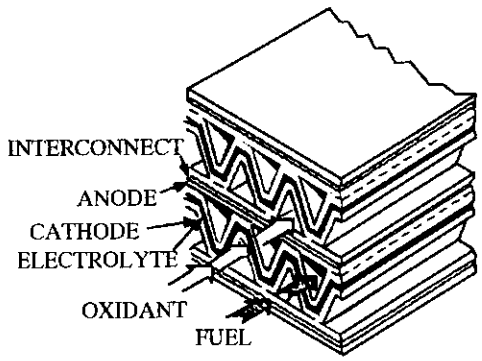

(b)

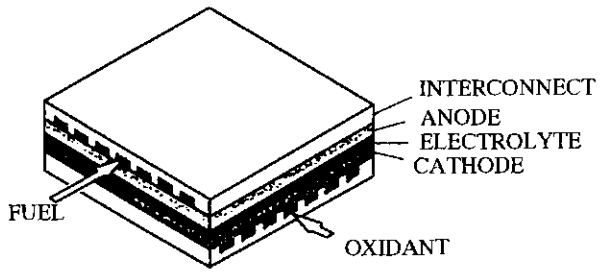

(c)

Figure 6-32. Tubular (a), monolithic (b) and flat plate (c) geometries of SOFCs.

separated by grooved bipolar plates or interconnects composed of Ni alloy–Al_2O_3, Ni alloy–CSZ (completely stabilized zirconia), or $LaCrO_3$ [177] that transport the fuel gas and the air, respectively as well as heat and current.

At the air electrode (cathode), oxygen combines with electrons, and the negatively charged oxygen ions are transported through the electrolyte via oxygen vacancies in the stabilized zirconia. To obtain reasonable transport rates, the temperature of the electrolyte must be at least 950 °C. At the fuel electrode (anode) a mixture of hydrocarbons and water reacts to hydrogen and carbon monoxide by internal reforming. The oxygen ions carried through the electrolyte oxidize the hydrogen and carbon monoxide to carbon dioxide and water releasing electrons that are transported back via an external circuit to the cathode (Fig. 6-31).

From this working principle of an SOFC it follows that the electrodes must have a high proportion of open porosity that will ensure fast and effective gas transport. On the other hand, the electrolyte transports only charged species, i.e. electrons and must thus be gastight. Increasingly work has been concentrated on producing the intricate shapes and compositions required for the PEN by plasma spraying technology. This includes the PSZ electrolyte [178–180], the cathodes [181, 182], cathodes and anodes [183] as well as the total PEN structure [184–187]. The interconnects of the planar SOFC, i.e. the bipolar plates, up to now hot pressed and rolled to a thickness of 3 mm and machined by ECM (electrochemical machining), can also be plasma-sprayed. Preliminary experiments were conducted with RF inductively-coupled plasma-sprayed $94Cr5Fe1Y_2O_3$ powders. The major challenge of economically producing bipolar plates by plasma spraying is concerned with producing a system of orthogonal grooves to carry the natural fuel/water mixture and air, respectively. Orthogonality is required to ensure effective cooling and a uniform temperature distribution that would considerably reduce thermal stresses across the PEN. A second problem is poisoning of the active cathode with nickel or chromium diffusing from the bipolar plate at the working temperature of 950 °C. To prevent this, a protective layer of $(La, Sr)CrO_3$ could be sprayed onto the cathode by VPS.

The functions of this protective ceramic layer include:

- electrical insulation of the bipolar plates,
- decrease of the thickness of the soldering gap between the ZrO_2 electrolyte and the bipolar plates,
- prevention of chromium oxide formation, and
- a barrier function against solid state diffusion of chromium oxide into the active internal cell volume.

These engineering challenges are not trivial and are compounded in monolithic SOFCs owing to the trapeziform gas channels (Fig. 6-32). For these reasons the tubular geometry of SOFCs is somewhat easier to realize and is thus closer to mass production [188]. A modern prototype of a tubular SOFC produced entirely by APS/VPS technology was recently developed in Japan [177]. Figure 6-33 shows a schematic illustration of the transaxial section of this tubular SOFC. On the surface of the outer support tube multiple cells are arranged: the anode consisting of Ni alloy/PSZ, followed by the Y–PSZ electrolyte, and on top the cathode consisting of a

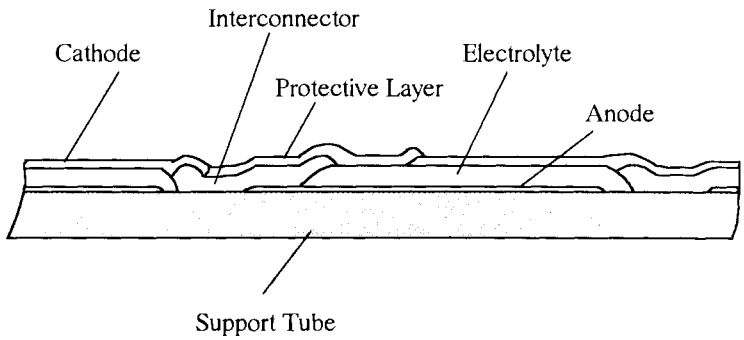

Figure 6-33. Prototype of an entirely plasma-sprayed tubular SOFC [177].

thanum composite oxide with perovskite structure, for example $LaCoO_3$. Integrated in this design are the interconnects of Ni alloy/Al_2O_3 coated by an Al_2O_3 protective coating to prevent oxidation of the Ni alloy. The electrodes and the interconnects were sprayed by APS, the very dense electrolyte by VPS. The support tube consisted of CSZ. This design has a very high fuel utilization of 87% and a high powder generation efficiency of 38%. A 1 kW prototype module, composed of 48 individual cells of the type shown in Fig. 6-33, was successfully operated for 3000 h.

Plasma-sprayed oxide electrocatalytic materials with spinel or perovskite structure are also being used as anode materials for water electrolyzers. Here an enormously important energy technology is being addressed as the production of hydrogen gas by electrolysis of water will be one of the mainstays of primary energy technology of the future. Electrocatalytic materials must conform to a complex set of stringent requirements [189]:

- chemical and electrochemical stability under operating conditions in alkaline water electrolysis,
- resistance to atomic oxygen,
- resistance to concentrated electrolyte solutions,
- resistance to working temperatures up to 150 °C,
- availability, and
- processability as layer or coating on metal electrodes.

Typical perovskites sprayed by VPS are (La, Sr) (Ni, Co)O_3 and, using an optimized Laval nozzle of low Mach number to generate a long laminar plasma jet, also the very attractive but highly parameter-sensitive Co_3O_4 [189, 190]. Using magnetite ore concentrates, magnetite–Co_3O_4 mixtures, and cobalt oxide, electrocatalytically active coatings for electrodes utilized in installations for water and sewage desinfection were produced by plasma spraying [191]. Even though the current efficiency is lower by 25–30% than for oxide–ruthenium–titanium anodes (ORTA), newly developed oxide–cobalt–titanium anodes (OCTA) have a higher chemical stability and an 8–12% higher productivity.

Prototype HT–SOFCs produced by Siemens in Germany operate between 800 and 1 000 °C, and use as cathode gases oxygen or air, as anode gases hydrogen, H_2/CO/CO_2 or $H_2/CO/CH_4$ gas mixtures. The planar fuel cells are gathered together in stacks reaching an electrical power output of 1 MW m^{-3} installed stack. Present problems to be addressed include:

- requirement of varying coating thicknesses on one bipolar plate,
- control of tolerances,
- solderability of the layers to obtain a stack,
- corrosion protection to 1100 °C,
- chemical resistance again the soldering material ($CaO–SiO_2–B_2O_3$ based), and
- high thermal shock resistance.

The market potential for SOFCs appears to be huge: 300–800 MW per annum in Europe, 1800 MW per annum in the USA, and 1100 MW per annum in Asia including Japan.

References

[1] W. Malléner, D. Stöver, *Proc. TS '90*, Essen **1990**, DVS 152, 3.
[2] G. Hägg, *Z. Phys. Chem.* **1929**, *6*, 221; **1931**, *12*, 33.
[3] W. Baumgart, Hard materials, in: *Process Mineralogy of Ceramic Materials* (eds. W. Baumgart, A. C. Dunham, G. C. Amstutz), Enke, Stuttgart, **1984**, p. 177.
[4] E. Lugscheider, M. Kuelkens, D. Hofmann, *Proc. 2nd Int. Conf. on Surface Eng.*, Stratford-on-Avon, UK, 16–18 June, **1987**, p. 423.
[5] E. Lugscheider, M. Kuelkens, *Advances in Thermal Spraying, Proc. ITSC*, Montreal, 8–12 Sept 1986 Canada **1986**, Welding Institute of Canada, p. 137.
[6] W. Jeitschko, H. Nowotny, F. Benesovsky, *Mh. Chem.* **1964**, *94*, 672.
[7] O. Knotek, E. Lugscheider, H. Reimann, *J. Vac. Sci. Technol.* **1975**, *12*(4), 75.
[8] S. Rangaswamy, H. Herman, Advances in Thermal Spraying, *Proc. 11th ITSC*, Montreal, Canada, 8–12 Sept **1986**, Welding Inst. of Canada 1986, p. 101.
[9] P. E. Chandler, A. R. Nicoll, *Proc. 2nd Int. Conf. on Surface Eng.*, Stratford-on-Avon, UK. 16–18 June, **1987**, 403.
[10] R. W. Smith, R. Novak, *PMI*, **1991**, *23*(3), 147.
[11] H. Kreye, D. Fandrich, H. H. Müller, G. Reiners, *Advances in Thermal Spraying, Proc. ITSC* **1986**, Welding Inst. of Canada, p. 121.
[12] D. Tu, S. Chang, C. Chao, C. Lin, *J. Vac. Sci. Technol.* **1985**, *A3*(6), 2479.
[13] R. B. Heimann, D. Lamy, T. Sopkow, *J. Can. Ceram. Soc.* **1990**, *59*(3), 49.
[14] C. D'Angelo, H. El Joundi, *Adv. Mat. Proc.* **1988**, *12*, 41.
[15] A. Wozniewski, *Proc. Int. Conf. Metallurg. Coatings*, ICMC, San Diego, 1–6 April, **1990**.
[16] R. Sivakumar, B. L. Mordike, *Surf. Coat. Technol.* **1989**, *37*, 139.
[17] M. E. Vinayo, F. Kassabji, J. Guyonnet, P. Fauchais, *J. Vac. Sci. Technol.* **1985**, *A3*(6), 2483.
[18] K. Hajmrle, M. Dorfman, *Mod. Dev. Powder Metall.* **1985**, *15/15*, 609.
[19] K. Kirner, *Schweißen Schneiden*, **1989**, *41*, 11.
[20] W. J. Lenling, M. F. Smith, J. A. Henfling, *Proc. 3rd NTSC, Thermal Spray Research and Applications*, Long Beach, CA, 20–25 May, **1990**, p. 451.
[21] K. Kamachi, S. Goda, S. Oki, M. Magome, K. Ueno, S. Sodeoka, G. Ueno, T. Yosioka, *Proc. 3rd NTSC, Thermal Spray Research and Applications*, Long Beach, CA 20–25 May, **1990**, p. 497.

[22] R. W. Smith, R. Novak, *PMI*, **1991**, *23*(4), 231.
[23] S. Shimizu, K. Nagai, *Weldi. Int.* **1991**, *5*, 12.
[24] H. Kolaska, K. Dreyer, *DIMA*, **1989**, 11.
[25] A. Sandt, *Schweißen Schneiden*, **1986**, *38*, 4.
[26] Z. Z. Mutasim, R. W. Smith, L. Sokol, *Thermal Spray Research and Applications, Proc. 3rd NTSC, Long Beach*, CA, 20–25 May, **1990**, p. 165.
[27] S. Fuji, T. Tajiri, A. Ohmori, *Proc. 14th ITSC '95*, Kobe, 22–26 May, **1995**, p. 839.
[28] C. Brunet, S. Dallaire, J. G. Sproule, *Advances in Thermal Spraying, Proc. ITSC* **1986**, Welding Inst. of Canada, p. 129.
[29] Z. Z. Mutasim, R. W. Smith, M. Mohanty, Drexel University, Personal Communication.
[30] R. W. Smith, D. Gentner, E. Harzenski, T. Robisch, *Thermal Spray Technology: New Ideas and Processes. Proc. NTSC '88*, Cincinnati, OH, 24–27 October, **1988**, p. 299.
[31] R. W. Smith, E. Lugscheider, P. Jokiel, U. Müller, J. Merz, M. Wilbert, *Proc. 5th NTSC*, Anaheim, CA, June **1993**.
[32] R. W. Smith, Z. Z. Mutasim, *J. Thermal Spray Technol.* **1992**, *1*(1), 57.
[33] R. W. Smith, M. R. Jackson, J. R. Rairden, J. S. Smith, *J. Met.* **1981**, *33*, 23.
[34] R. W. Smith, E. Harzenski, T. Robisch, *Proc. 12th ITSC*, London, UK, June **1989**.
[35] G. Veilleux, R. G. Saint-Jacques, S. Dallaire, *Thin Solid Films* **1987**, *154*, 91.
[36] H. Jungklaus, E. Lugscheider, R. Limbach, R. W. Smith, *Proc. 13th ITSC '92*, Orlando, FL, **1992**, p. 679.
[37] S. G. Cliche, S. Dallaire, *Thermal Spray Research and Applications, Proc. 3rd NTSC, Long Beach*, CA, 20–25 May, **1990**, p. 761.
[38] P. Vuoristo, K. Niemi, B. Jouve, T. Stenberg, T. Mäntylä, L.-M. Berger, M. Nebelung, W. Hermel, *Proc. 14th ITSC '95*, Kobe, 2–26 May, **1995**, 699.
[39] S. Thiele, R. B. Heimann, L.-M. Berger, M. Nebelung, K. Schwarz, *J. Mater. Sci. Lett.* 1996, 15(8), 683.
[40] K. S. Fessenden, C. V. Cooper, L. H. Favrow, A. P. Matarese, T. P. Slavin, *Proc. 3rd NTSC, Thermal Spray Research and Applications*, Long Beach, CA, 20–25 May, **1990**, 611.
[41] H. E. Hintermann, *J. Vac. Sci. Technol.* **1984**, *2*, 816.
[42] E. R. Buchanan, *Turbomachinery Int.* **1987**, *28*(1), 25.
[43] R. J. Ortolano, *Turbomachinery Int.* **1983**, *April*, 19.
[44] *Development of low-pressure coatings resistant to steam-borne corrodents*, EPRI Project CS-3139, Vol. 1, June, **1983**.
[45] J. Qureshi, A. Levy, B. Wang, *J. Vac. Sci. Technol.* **1986**, *A4*(6), 2638.
[46] W. J. Sumner, J. H. Vogan, R. J. Lindinger, *Proc. Am. Power Conf.*, 22–24 April, **1985**, p. 196.
[47] U. Menne, A. Mohr, M. Bammer, C. Verpoort, K. Ebert, R. Baumann, *Proc. TS '93, Aachen* **1993**, DVS 152, 280.
[48] S. T. Wlodek, *EPRI Workshop on Solid Particle Erosion of Steam Turbines*, Chattanooga, TN, USA, **1985**.
[49] I. G. Wright, *Mater. Sci. Eng.* **1987**, *88*, 261.
[50] I. G. Wright, V. Nagarajan, J. Stringer, *Oxid. Met.* **1986**, *25*(3/4), 175.
[51] L. F. Albright, C. F. McConnell, K. Welther, *Proc. ACS 175th National Meeting*, Anaheim, CA, USA, 12–17 March, **1978**, p. 175.
[52] L. F. Albright, C. F. McConnell, *Proc. ACS 175th National Meeting*, Anaheim, CA, USA, 12–17 March, **1978**, p. 205.
[53] G. L. Swales, in: *Behaviour of High temperature Alloys in Agressive Environments* (Eds. I. Kirman, J. B. Marriott, M. Merz), The Metals Society, London, **1980**, p. 45.
[54] S. M. Brown, L. F. Albright, Chapter 17 in: *Industrial and Laboratory Pyrolysis* (Eds. L. F. Albright, B. L. Crynes), American Chemical Society, Washington, **1976**, 175.
[55] S. Dallaire, B. Champagne, in: *Modern Development in Powder Metallurgy* (Eds. E. N. Aqua, Ch. I. Whitman), **1985**, *17*, 589.
[56] P. Schwarzkopf, F. W. Glaser, *Z. Metall.* **1953**, *44*, 353.
[57] B. Champagne, S. Dallaire, *J. Vac. Sci. Technol.* **1985**, *A3*(6), 2373.
[58] T. W. Kuijpers, J. H. Zaat, *Metals Technol. March* **1974**, 142.
[59] E. Lugscheider, H. Jungklaus, P. Remer, J. Knuuttila, *Proc. 14th ITSC*, Kobe, 22–26 May, **1995**, p. 833.

[60] H. Herman, C. C. Berndt, H. Wang, Plasma Sprayed Ceramic Coatings, Chapter 5 in: *Ceramic Films and Coatings* (Eds. J. B. Wachtman, R. A. Haber), Noyes: Park Ridge, NJ, USA, **1993**, p. 131.
[61] L. Brown, H. Herman, R. K. MacCrone, *Advances in Thermal Spraying*, Pergamon, Toronto, **1986**, p. 507.
[62] R. B. Heimann, D. Lamy, T. N. Sopkow, *Proc. 3rd NTSC, Thermal Spray Research and Applications*, Long Beach, CA, USA, 20–25 May, **1990**, p. 491.
[63] R. Kingswell, D. S. Rickerby, K. T. Scott, S. J. Bull, *Proc. 3rd NTSC, Thermal Spray Research and Applications*, Long Beach, CA, USA, 20–25 May, **1990**, p. 179.
[64] T. Chon, G. A. Bancke, H. Herman, H. Gruner, *Thermal Spray-Advances in Coatings Technology*, ASM International, Cleveland, OH, USA, **1988**, p. 329.
[65] H. Hannotiau, J. Leunen, J. Sleurs, S. Heusdains, H. Tas, *1st Int. Conf. Plasma Surface Eng.*, Garmisch-Partenkirchen, Germany, 19–23 September, **1988**.
[66] A. Petitbon, D. Guignot, U. Fischer, J.-M. Guillemot, *Mater. Sci. Eng.* **1989**, *A121*, 545.
[67] E. D. Kirbach, M. Stacey, Personal communication, Forintek Canada Corp., Western Laboratory, Vancouver, BC, Canada, **1989**.
[68] H. Rump, W. Möhler, *Keram. Z.* **1995**, *47*(4), 284.
[69] T. Gößmann, H. G. Schütz, D. Stöver, H. P. Buchkremer, D. Jäger, *Proc. 3rd NTSC, Thermal Spray Research and Applications*, Long Beach, CA, USA, 20–25 May, **1990**, p. 503.
[70] J. Beczkowiak, K. Mundinger, *Proc. 13th ITSC*, London, UK, **1989**, p. 94.
[71] I. G. Wright, V. Nagarajan, J. Stringer, *Oxid. Met.* **1986**, *25*(3/4), 175.
[72] I. Kvernes, E. Lugscheider, *PMI*, **1992**, *24*(1), 7.
[73] D. Gansert, E. Lugscheider, U. Müller, *Proc. 3rd NTSC, Thermal Spray Research and Applications*, Long Beach, CA, USA, 20–25 May, **1990**, p. 517.
[74] N. F. Seliverstov, V. A. Ryabin, M. Ya. Berezhneva, A. B. Chudinov, Yu. S. Borisov, *Proc. TS '93*, Aachen **1993**, DVS 152, 442.
[75] L. N. Kozina, Yu. P. Revyakin, *Izvest. AN SSSR, Metall.* **1970**, 56.
[76] D. J. Varacalle, M. G. Jacox, L. B. Lundberg, J. R. Hartenstine, H. Herman, G. A. Bancke, W. Riggs, *J. Surf. Coat. Technol.* **1993**, *December*.
[77] D. J. Varacalle, R. A. Neiser, M. F. Smith, *Proc. 13th ITSC, Thermal Spray: International Advances in Coatings Technology*, Orlando, FL, USA, May **1992**.
[78] E. R. Buchanan, A. Sickinger, *Proc. 1994 NTSC*, Boston, MA, USA, 20–24 June, **1994**.
[79] T. McKechnie *et al. Proc. 1993 NTSC*, Orlando, FL, USA, 7–11 June, **1993**.
[80] W. Cai, H. Liu, A. Sickinger, E. Muehlberger, D. Bailey, E. J. Lavernia, *J. Thermal Spray Technol.* **1994**, *3*(2), 135.
[81] J. M. Houben, Relation of the adhesion of plasma sprayed coatings to the process parameters size, velocity and heat content of the spray particles. Ph.D. Thesis, Technical University Eindhoven, The Netherlands, **1988**.
[82] D. J. Varacalle, L. B. Lundberg, B. G. Miller, W. L. Riggs, *Proc. 14th ITSC*, Kobe, Japan, 22–26 May, **1995**, p. 377.
[83] P. D. Prichard, R. L. McCormick, Z. Z. Mutasim, R. W. Smith, *Proc. Composite Forming Symp., AIME Winter Meeting*, Anaheim, CA, USA, February **1990**.
[84] H.-D. Steffens, H.-M. Höhle, E. Ertürk, *Thin Solid Films* **1980**, *73*, 19.
[85] E. Lugscheider, P. Lu, B. Hauser, D. Jäger, *J. Surf. Coat. Technol.* **1987**, *32*, 215.
[86] M. L. Thorpe, R. H. Unger, *Advances in Thermal Spraying, Proc. ITSC* **1986**, Welding Inst. of Canada, p. 3.
[87] M. Müller, F. Gitzhofer, R. B. Heimann, M. I. Boulos, *Proc. NTSC '95*, Houston, TX, USA, 11–15 Sept, **1995**, p. 567.
[88] R. Rairden, M. R. Jackson, M. F. Henry, *Proc. 10th ITSC, Essen* **1983**, DVS 80, 205.
[89] M. G. Hebsur, R. V. Miner, *Mater. Sci. Eng.* **1986**, *83*, 239.
[90] C. A. Barrett, C. E. Lowell, *Oxid. Met.* **1977**, *11*, 199.
[91] J. Gayda, T. P. Gabb, R. V. Miner, *J. Fatigue* **1986**, *8*(4), 217.
[92] M. G. Hebsur, R. V. Miner, *Thin Solid Films* **1987**, *147*, 143.
[93] S. M. Merchant, M. R. Notis, *Mater. Sci. Eng.* **1984**, *66*, 47.
[94] K. Noguchi, M. Nishida, A. Chiba, J. Takeuchi, Y. Harada, *Proc. 14th ITSC*, Kobe, Japan, 22–26 May, **1995**, p. 459.

[95] K. E. Spear, *J. Am. Ceram. Soc.* **1989**, *72*, 171.
[96] P. K. Bachmann, D. Leers, H. Lydtin, *Diamond Relat. Mat.* **1991**, *1*, 1.
[97] K. Kurihara, K. Sasaki, M. Kawarada, N. Koshino, *Appl. Phys. Lett.* **1988**, *52*, 437; also *Fujitsu Sci. Technol. J.* **1989**, *25*, 44.
[98] E. Lugscheider, U. Müller, F. Deuerler, W. Schlump, *Proc. TS '93*, Aachen **1993**, DVS 152, p. 19.
[99] R. B. Heimann, *Proc. Adv. Mater.* **1991**, *1*, 181.
[100] E. Lugscheider, U. Müller, F. Deuerler, W. Schlump, P. Jokiel, P. Remer, *Proc. 13th Intern. Plansee Seminar*, Reutte, Germany **1993**, *3*, p. 287.
[101] E. Lugscheider, U. Müller, *Ingenieur-Werkstoffe*, **1992**, *4*(7/8), 42.
[102] F. Matsumoto, S. Kato, Y. Tomii, *Proc. 14th ITSC*, Kobe, Japan, 20–26 May, **1995**, 821.
[103] S. Matsumoto, *Mater. Res. Soc. Symp. Proc.* **1988**, *EA-15*, 119.
[104] M. Murakawa, S. Takeuchi, Y. Hirose, *Mater. Res. Soc. Symp. Proc.* **1989**, *EA-19*, 63.
[105] K. A. Snail, *Inside R&D*, **1991**, *10*(23), 1.
[106] D. G. Goodwin, *Mater. Res. Soc. Symp. Proc.* **1989**, *EA-19*, 153.
[107] W. A. Weimer, F. M. Cerio, C. E. Johnson, *J. Mater. Res.* **1991**, *6*, 2134.
[108] D. A. Spera, S. J. Grisaffe, *NASA Technical Memorandum TMX-2664*. National Technical Information Service, Springfield, VA, USA, **1973**.
[109] R. Sivakumar, B. L. Mordike, *Surf. Coat. Technol.* **1988**, *37*, 139.
[110] *Neue Materialien für Schlüsseltechnologien des 21. Jahrhunderts*, MaTech, Bundesmin. für Forschung und Technologie, Bonn, August **1994**.
[111] R. A. Miller, *Surf. Coat. Technol.* **1987**, *30*, 1.
[112] H. Yajima, Y. Kimura, T. Yoshioka, *Proc. 14th ITSC, Kobe*, Japan 22–26 May, **1995**, p. 621.
[113] P. E. Hodge, R. A. Miller, M. A. Gedwill, *Thin Solid Films*, **1980**, *73*, 447.
[114] E. P. Butler, *Mater. Sci. Technol.* **1985**, *1*(6), 417.
[115] H. G. Scott, *J. Mater. Sci.* **1975**, *10*(9), 1527.
[116] K. M. Jasim, R. D. Rawlings, D. R. F. West, *Mater. Sci. Technol.* **1992**, *8*(1), 83.
[117] B. C. Wu, E. Chang, S. E. Chang, D. Tu, *J. Am. Ceram. Soc.* **1989**, *72*(2), 212.
[118] N. Iwamoto, N. Umesaki, M. Kamai, G. Ueno, *Proc. TS '90*, Essen **1990**, DVS 130, 99.
[119] J. E. Restall, *Proc. 5th Intern. Symp. on Superalloys*, Champion, PA, USA, 7–11 Oct, **1984**, p. 721.
[120] T. N. Rhys-Jones, *Corrosion Science* **1989**, *29*(6), 623.
[121] D. M. Comassar, *Metal Finishing* **1991**, *March*, 39.
[122] R. W. Smith, W. F. Schilling, H. M. Fox, *Trans. ASME* **1981**, *103*, 146.
[123] S. Stecura, *Ceram. Bull.* **1982**, *61*(2), 256.
[124] G. C. Chang, W. Phucharoen, R. A. Miller, *Surf. Coat. Technol.* **1987**, *30*, 13.
[125] R. A. Miller, *NASA Technical Memorandum TM 100283*, **1988**.
[126] R. A. Miller, *J. Am. Ceram. Soc.* **1984**, *67*, 517.
[127] D. L. Ruckle, *Thin Solid Films* **1980**, *73*, 455.
[128] A. Feuerstein, W. Dietrich, E. Muehlberger, Ph. Meyer, *Proc. Conf. High Temp. Alloys for Gas Turbines and Other Applic.*, Liege, Belgium, 6–9 Oct, **1986**, p. 1227.
[129] F. N. Longo, H. Florant, *Proc. 8th ITSC*, Miami, FL, USA, Sept **1976**.
[130] K. Cushnie, J. A. E. Bell, G. D. Smith, *Proc. 3rd NTSC, Thermal Spray Research and Applications*, Long Beach, CA, USA, 20–25 May, **1990**, 539.
[131] H.-D. Steffens, Z. Babiak, U. Fischer, *Proc. 2nd Intern. Conf. on Surface Eng.*, Stratford-upon-Avon, UK, 16–18 June, **1987**, p. 471.
[132] M. Gramlich, H.-D. Steffens, *Working Group Session 'Ceramic Coatings'*, German Ceramic Society (DKG), Heilbronn, Germany, 8–9 June, **1994**.
[133] G. Eckold, I. M. Buckley-Golder, K. T. Scott, *Proc. 2nd Intern. Conf. Surface Eng.*, Stratford-on-Avon, UK, 16–18 June, **1987**, p. 433.
[134] R. B. Heimann, D. Lamy, V. E. Merchant, *Trans. 17th CUICAC Workshop*, (Ed. R. B. Heimann), Laval University, Québec City, Québec, Canada, 2 Oct, **1991**.
[135] I. Zaplatynsky, NASA Technical Memorandum 82830, *Proc. Int. Conf. Metall. Coatings and Process Technology*, San Diego, CA, USA, 5–8 April, **1982**.
[136] A. Adamski, R. McPherson, *Advances in Thermal Spraying, Proc. ITSC* **1986**, Welding Inst. of Canada, p. 555.

[137] T. R. Anthony, H. E. Cline, *J. Appl. Phys.* **1977**, *48*(9), 3888.
[138] H. E. Cline, *J. Appl. Phys.* **1981**, *52*(1), 443.
[139] J.-H. Shieh, S.-T. Wu, *Appl. Phys. Lett.* **1991**, *59*(12), 1512.
[140] K. M. Jasim, R. D. Rawlings, D. R. F. West, *J. Mater. Sci.* **1992**, *27*, 3903.
[141] K. M. Jasim, D. R. F. West, W. M. Steen, R. D. Rawlings, *Proc. 7th Intern. Congr. on Applic. Lasers and Electrooptics (ICALEO '88)* (ed. G. Bruck), Springer, Berlin, **1988**, p. 17.
[142] H. Uchikawa, H. Hagiwara, M. Shirasaka, H. Yamane, *Proc. Surf. Eng. Intern. Conf.*, Tokyo, Japan, 18–22 Oct, **1988**, p. 45.
[143] M. Yoshida, K. Abe, T. Aranami, Y. Harada, *Proc. 14th ITSC*, Kobe, Japan, 22–26 May, **1995**, p. 785.
[144] K. Søballe, Hydroxyapatite ceramics coating for bone implant fixation. Mechanical und histological studies in dogs. *Acta Orthop. Scand.* **1993**, *64*, 58.
[145] C. P. A. T. Klein, P. Patka, H. B. M. vanderLubbe, J. G. C. Wolke, K. deGroot, *J. Biomed. Mater. Res.* **1991**, *25*, 53.
[146] D. P. Rivero, J. Fox, A. K. Skipor, R. M. Urban, J. O. Galante, *J. Biomed. Mater. Res.* **1988**, *22*, 191.
[147] K. deGroot, R. T. G. Geesink, C. P. A. T. Klein, P. Serekian, P., *J. Biomed. Mater. Res.* **1987**, *21*, 1375.
[148] B. Simons, in: *PLATIN-Seminar, Innovative Anwendungen von Plasma-Technologien in der Medizintechnik*, Wuppertal, Germany, 14. September **1995**.
[149] O. Ohtsuka, M. Matsuura, N. Chida, M. Yoshinari, T. Sumii, T. Dérand, *Surf. Coat. Technol.* **1994**, *65*, 224.
[150] K. Yamashita, T. Arashi, K. Kitagaki, S. Yamada, T. Umegaki, K. Ogawa, *J. Am. Ceram. Soc.* **1994**, *77*, 2401.
[151] T. Kokubo *et al.* in: *Bioceramics Vol. 4* (Proceedings of the 4th International Symposium on Ceramics in Medicine, London, UK, September 1991) (ed. W. Bonfield, G. W. Hasting, K. E. Tanner) Butterworth-Heinemann, Oxford, UK, **1991**, p. 113.
[152] P. Ducheyne, S. Radin, M. Heughebaert, J. C. Heughebaert, *Biomaterials* **1990**, *11*, 244.
[153] M. Weinlaender, J. Beumer, E. B. Kenney, P. K. Moy, F. Adar, *J. Mater. Sci.: Mater. Med.* **1992**, *3*, 397.
[154] A. J. Sturgeon, M. D. F. Harvey, M. D. F., *Proc. 14th ITSC '95*, Kobe, Japan, 22–26 May, **1995**, 933.
[155] T. A. Vu, R. B. Heimann, *Eur. J. Mine.* in press.
[156] K. de Groot, *J. Ceram. Soc. Jpn.: Int. Edt.* **1991**, *99*, 917.
[157] Ch. Zimmermann, Histologische und histomorphometrische Untersuchungen am Interface Apatit-beschichteter Titan-Implantate, Dissertation University of Heidelberg **1992**.
[158] E. Lugscheider, M. Knepper, B. Heimberg, A. Dekker, C. J. Kirkpatrick, *J. Mater. Sci.: Mater. Med.* **1994**, *5*, 371.
[159] E. Lugscheider, M. Knepper, *Proc. TS '93*, Aachen **1993**, DVS 152, 82.
[160] J. G. C. Wolke, J. M. deBlieck-Hogervorst, W. J. A. Dhert, C. P. A. T. Klein, K. deGroot, *J. Thermal Spray Technol.* **1992**, *1*, 75.
[161] M. J. Filiaggi, N. A. Coombs, R. M. Pilliar, *J. Biomed. Mater. Res.* **1991**, *25*, 1211.
[162] J. H. C. Lin, M. L. Liu, C. P. Ju, *J. Mater. Sci.: Mater. Med.* **1994**, *5*, 279.
[163] K. de Groot, *Ann. NY Acad. Sci.* **1988**, *523*, 227.
[164] H. Ji, C. B. Ponton, P. M. Marquis, *J. Mater. Sci.: Mater. Med.* **1992**, *3*, 283.
[165] J. Weng, *J. Mater. Sci. Lett.* **1994**, *13*, 159.
[166] D. M. Liu, H. M. Chou, J. D. Wu, *J. Mater. Sci.: Mater. Med.* **1994**, *5*, 147.
[167] C. P. A. T. Klein, P. Patka, J. G. C. Wolke, J. M. A. deBlieck-Hogervorst, K. de Groot, *Biomaterials* **1994**, *15*, 146.
[168] H. Ogushi, K. Ishikawa, S. Ojima, Y. Hirayama, K. Seto, G. Eguchi, *Biomaterials* **1992**, *13*, 471.
[169] T. Kameyama, M. Ueda, A. Motoe, K. Ohsaki, H. Tanizaki, K. Iwasaki, *Proc. 1st Intern. Conf. on Processing Materials for Properties*, (ed. H. Henein, T. Oki), The Minerals, Metals and Materials Soc. **1993**, p. 1097.
[170] D. O. Welch, V. J. Enery, D. E. Cox, *Nature*, **1987**, *327*, 278.
[171] L. Pawlowski, A. Hill, R. McPherson, D. Garvie, Z. Przelozny, T. Finlayson, *Proc. 3rd*

NTSC, Thermal Spray Research and Applications, Long Beach, CA, USA, 20–25 May, **1990**, p. 641.
[172] E. Lugscheider, T. Weber, *Proc. 3rd NTSC, Thermal Spray Research and Applications*, Long Beach, CA, USA, 20–25 May, **1990**, p. 635.
[173] A. Shah, S. Patel, E. Narumi, D. T. Shaw, *Appl. Phys. Lett.* **1990**, *57*(14), 1452.
[174] H. Zhu, Y. C. Lau, E. Pfender, *Proc. 9th Int. Symp. Plasma Chem.*, Pugnochiuso **1989**, *876*, 1497.
[175] H. Zhu, Y. C. Lau, E. Pfender, *J. Appl. Phys.* **1991**, *69*(5), 3404.
[176] A. Shah, T. Haugan, S. Witanachi, S. Patel, T. Shaw, *Proc. Mat. Res. Soc. Symp.*, Boston, MA, USA, **1989**, p. 747.
[177] A. Notomi, H. Hisatome, *Proc. 14th ITSC*, Kobe, Japan, 22–26 May, **1995**, p. 79.
[178] M. Scagliotti, F. Parmigiani, G. Samoggia, G. Lanzi, D. Richon, *J. Mater. Sci.* **1988**, *23*, 3764.
[179] C. L. Curtis, D. T. Gawne, N. Priestnall, *Proc. 1993 NTSC*, Anaheim, CA, USA, June **1993**, p. 519.
[180] A. R. Nicoll, G. Barbezat, A. Salito, *SOFC-Seminar*, Yokohama, Japan, Feb **1992**.
[181] Z. Li, W. Mallener, L. Fuerst, D. Stöver, F.-D. Scherberich, *Proc. 1993 NTSC*, Anaheim, CA, USA, June **1993**, p. 343.
[182] L.-W-Tai, P. A. Lessing, *J. Am. Ceram. Soc.* **1991**, *74*(3), 501.
[183] R. Okiai, S. Yoshida, I. Kaji, *1st Int. Symp. on SOFC*, Nagoya, Japan, 13–14 Nov, **1989**, p. 191.
[184] I. Kaji, S. Yoshida, N. Nagata, T. Nakajima, Y. Seino, *2nd Int. Symp. on SOFC*, Nagoya, Japan, **1991**, p. 221.
[185] R. Henne, G. Schiller, *Foschungsverbund Sonnenenergie, 'Themen 94/95'*, **1994**, 89.
[186] R. Henne, E. Fendler, M. Lang, *Proc. 1st Europ. Solid Oxide Fuel Cell Forum*, Lucerne, Switzerland, 3–7 Oct, **1994**, *2*, 617.
[187] W. Mallener, K. Wippermann, H. Jansen, Z. Li, D. Stöver, *Proc. ITSC '92*, Orlando, FL, USA, 28 May–5 June, **1992**, p. 835.
[188] K. Minazawa, K. Toda, S. Kaneko, N. Murakami, A. Notomi, *MHI Technical Bulletin*, **1991**, *28*(1), 41.
[189] R. Henne, M. v. Bradke, G. Schiller, W. Schnurnberger, W. Weber, *Proc. 12th ITSC '89*, London, UK, 4–9 June, **1989**, 175.
[190] G. Schiller, R. Henne, V. Borck, *J. Thermal Spray Technol.* **1995**, *4*(2), 185.
[191] Yu. Borisov, A. Murashov, A. Ilienko, V. Balakin, V. Slipchenko, A. Slipchenko, V. Maksimov, *Proc. 14th ITSC*, Kobe, Japan, 22–26 May, **1995**, p. 141.